Continuous endosomes form functional subdomains and orchestrate rapid membrane trafficking in trypanosomes

Authors:

Fabian Link[1], Alyssa Borges[1], Oliver Karo[1], Marvin Jungblut[2], Thomas Müller[1], Elisabeth Meyer-Natus[1], Timothy Krüger[1], Stefan Sachs[2], Nicola G. Jones[1], Mary Morphew[3], Markus Sauer[2], Christian Stigloher[4], J. Richard McIntosh[3], Markus Engstler[1]

Affiliations:

[1]Department of Cell & Developmental Biology, Biocentre, University of Würzburg, 97074 Würzburg, Germany

[2]Department of Biotechnology & Biophysics, Biocentre, University of Würzburg, 97074 Würzburg, Germany

[3]Molecular, Cellular & Developmental Biology, University of Boulder, Colorado, USA

[4] Imaging Core Facility, Biocentre, University of Würzburg, 97074 Würzburg, Germany

Corresponding authors: Markus Engstler (markus.engstler@uni-wuerzburg.de)

Keywords:

Membrane recycling, African trypanosomes, Endocytosis, Rab proteins, Tokuyasu, Tomography

Abstract

Endocytosis is a common process observed in most eukaryotic cells, although its complexity varies among different organisms. In *Trypanosoma brucei*, the endocytic machinery is under special selective pressure because rapid membrane recycling is essential for immune evasion. This unicellular parasite effectively removes host antibodies from its cell surface through hydrodynamic drag and fast endocytic internalization. The entire process of membrane recycling occurs exclusively through the flagellar pocket, an extracellular organelle situated at the posterior pole of the spindle-shaped cell. The high-speed dynamics of membrane flux in trypanosomes do not seem compatible with the conventional concept of distinct compartments for early, late and recycling endosomes. To investigate the underlying structural basis for the remarkably fast membrane traffic in trypanosomes, we employed advanced techniques in light and electron microscopy to examine the three-dimensional architecture of the endosomal system. Our findings reveal that the endosomal system in trypanosomes exhibits a remarkably intricate structure. Instead of being compartmentalized, it constitutes a continuous membrane system, with specific functions of the endosome segregated into membrane subdomains enriched with classical markers for early, late, and recycling endosomes. These membrane subdomains can partly overlap or are interspersed with areas that are negative for endosomal markers. This continuous endosome allows fast membrane flux by facilitated diffusion that is not slowed by multiple fission and fusion events.

60 # Introduction

61 Endocytosis research has traditionally focused on a limited number of organisms, primarily
62 opisthokonts (including yeast and humans). Recently, using the extensive genetic and cell
63 biological resources now available for studying numerous other organisms, studies on protists
64 such as *Dictyostelium*, *Giardia*, *Toxoplasma* or trypanosomes have revealed remarkable
65 deviations from the hitherto existing understanding of the processes of endo- and exocytosis
66 described in textbooks (reviewed in Benchimol and de Souza, 2022; Link et al., 2021;
67 McGovern et al., 2021; Vines and King, 2019). Looking at the distinct evolutionary solutions
68 for endosomal recycling across different branches of the eukaryotes, these protists, and
69 especially the parasites among them, are of particular interest.
70 Throughout their life cycle, parasites often encounter a series of inherently hostile
71 environments. The arms race between the parasite and its host has resulted in coevolutionary
72 processes characterized by intense reciprocal selective pressures. Although parasite and host
73 use similar basic cell biological pathways, parasites have often optimised these, either to
74 achieve maximum efficiency or to establish additional functions. In this regard, the endocytosis
75 and membrane recycling mechanisms observed in African trypanosomes serve as a remarkable
76 illustration of the exceptional functional adaptations exhibited by parasites in response to their
77 specific host environments.
78
79 *Trypanosoma brucei* is a representative of the group Discoba, which diverged before the
80 appearance of opisthokonts (Burki et al., 2020; Strassert et al., 2021). *T. brucei* is an exclusively
81 extracellular parasite, that resists the harsh conditions within the bloodstream, interstitial fluids
82 and lymph and thus thrives in the body fluids of its vertebrate host. Additionally, the cells have
83 adapted to entirely distinct, yet equally challenging environments within the transmitting insect
84 vector, *Glossina* (tsetse fly). Within the midgut of the fly, the trypanosomes proliferate to very
85 high densities and, following a several week long journey, attach to the insect salivary glands
86 before being injected back into the host skin during the bloodmeal of the tsetse (Rose et al.,
87 2020).
88
89 The extracellular lifestyle of *T. brucei* renders the parasite vulnerable to constant attacks by the
90 host's immune system. In response, these parasites have evolved a protective surface coat
91 covering the entire plasma membrane (Cross, 1975). This coat comprises a single type of variant
92 surface glycoprotein (VSG) and forms the basis of antigenic variation (Mugnier et al., 2016).
93 *T. brucei* possesses hundreds of VSG genes that encode structurally similar yet antigenically

distinct proteins (Taylor and Rudenko, 2006). However, only one VSG gene is expressed at a time, originating from a polycistronic expression site located at the telomere of the chromosomes (Becker et al., 2004; Chaves et al., 1999). The stochastic switching to the expression of a new VSG guarantees that the parasites remain ahead of the host immune response.

Antigenic variation is not the sole defense strategy employed against the host´s immune reaction. During immune attack, parasites actively remove anti-VSG antibodies from their cell surface. This process of antibody clearance is driven by hydrodynamic drag forces resulting from the continuous directional movement of trypanosomes (Engstler et al., 2007). The VSG-antibody complexes on the cell surface are dragged against the swimming direction of the parasite and accumulate at the posterior pole of the cell. This region harbours an invagination in the plasma membrane known as the flagellar pocket (FP) (Gull, 2003; Overath et al., 1997). The FP, which marks the origin of the single attached flagellum, is the exclusive site for endo- and exocytosis in trypanosomes (Gull, 2003; Overath et al., 1997). Consequently, the accumulation of VSG-antibody complexes occurs precisely in the area of bulk membrane uptake. For the process of antibody clearance to function efficiently, several conditions must be met. The VSG coat must be densely packed to prevent immune recognition of non-variant surface proteins, VSG must be highly mobile to allow the drag forces to take effect, and endocytosis must be sufficiently rapid to internalize the VSG-antibody complexes effectively. Furthermore, endosomal sorting and membrane recycling must keep pace with the bulk membrane uptake to maintain membrane balance. In fact, the VSG coat is as densely packed as physically possible (Hartel et al., 2016) and VSG molecules possess a flexible C-terminal domain attached via a GPI-anchor to the outer leaflet of the plasma membrane (reviewed in Borges et al., 2021). This lipid anchoring enables the highly dynamic behaviour of the VSG coat (Bartossek et al., 2017), further facilitated by N-glycans that insulate VSG molecules, thereby minimizing protein-protein interactions (Hartel et al., 2016). VSG molecules exhibit diffusion on the plasma membrane with coefficients that enable fast randomization (Hartel et al., 2016; Schwebs et al., 2022). This rapid VSG diffusion is precisely balanced with membrane recycling kinetics, with one surface equivalent being internalized and recycled within 12 minutes (Engstler et al., 2004). This exceptionally fast endocytosis is crucial for antibody clearance.

To summarize, *T. brucei* has evolved a series of interconnected cell biological adaptations in order to evade the immune system, ranging from a highly polarized cell structure and constant

directional motion to the generation of a variable, densely packed yet highly mobile cell surface coat, as well as an unusually rapid endocytosis machinery. The strong selective pressure acting on trypanosomes has led to the integration and coordination of seemingly unrelated features, such as cell motility, surface protein dynamics, clathrin-mediated endocytosis, protein sorting, and membrane recycling. This illustrates the extraordinary cell biology of parasitic protozoa, which offers functional linkages beyond that of yeast or mammalian cells.

In *T. brucei*, the process of endocytosis (reviewed in Link et al., 2021) begins with the formation of clathrin-coated vesicles (CCVs) at the flagellar pocket membrane (Allen et al., 2003; Morgan et al., 2001). Subsequently, both membrane-bound VSG and fluid-phase cargo pass through early endosomes (EE) (Engstler et al., 2004; Grünfelder et al., 2003). From this compartment, both either move directly to the recycling endosomes (RE) and return to the cell surface or first pass from the EE to the late endosomes (LE) before returning to the surface via the RE (Engstler et al., 2004). Alternatively, fluid-phase cargo can be directed from LEs to the lysosome for degradation (Engstler et al., 2004). In comparison, less is known about the biosynthetic pathway to the lysosome. Endogenous proteins like TbCatL, a soluble thiol protease, and p67, a membrane glycoprotein, are segregated from secretory cargo in the Golgi apparatus. They are then transported out of the Golgi, probably in a clathrin-dependent manner (Tazeh et al., 2009). An alternative route to the lysosome was discovered by disrupting transport signals in endogenous proteins, for example by blocking of GPI anchor addition to VSGs (Triggs and Bangs, 2003).

Similar to other eukaryotic organisms, the trafficking process through various endosomal compartments is regulated by a core set of three small Rab-GTPases (Ackers et al., 2005). TbRab5 and TbRab11 are responsible for controlling trafficking through the early and recycling endosomes, respectively (Field et al., 1998; Hall et al., 2005; Pal et al., 2003). TbRab7 plays a role in regulating late endocytic trafficking to the lysosome, but does not appear to be involved in the biosynthetic trafficking of either native lysosomal proteins or default reporters (Silverman et al., 2011). TbRab5A-positive endosomal structures have been described by immuno-electron microscopy as circular or elongated cisternae, while TbRab7-positive structures exhibit an irregular shape (Engstler et al., 2004; Grünfelder et al., 2003; Overath and Engstler, 2004). Additionally, TbRab11-positive structures are characterized as either elongated cisternae or disk-shaped exocytic carriers (Grünfelder et al., 2003). Apart from exocytic carriers, the exocyst is currently the only proposed mediator of exocytosis (Boehm et al., 2017).

A thorough examination of the kinetics of endosomal recycling has validated the rapid passage through various endosomal compartments (Engstler et al., 2004; Grünfelder et al., 2003). However, these analyses have not addressed how the kinetics can be reconciled with the occurrence of multiple fission and fusion events that are thought to accompany endosomal transport through these compartments.

Here, we have employed a comprehensive set of techniques to scrutinize the ultrastructure of specific endosomal subdomains in *T. brucei*. In addition to utilizing electron tomography, super-resolution fluorescence microscopy and colocalization analysis, we have introduced Tokuyasu sectioning for 3D immuno-electron microscopy. These tools allowed us to elucidate the structural basis for the remarkable speed of endosomal recycling in trypanosomes.

177 # Results

178 **The endosomal apparatus of *T. brucei* is a large intricate structure**

179 In order to generate an overview of the endosomal ultrastructure in bloodstream form (BSF)
180 trypanosomes, we performed electron tomography after fluid phase cargo uptake assays with
181 horseradish peroxidase (HRP) and ferritin (Figure 1, Supplementary movie 1). Fluid phase
182 cargo was selected as it ensures a comprehensive labelling of all endosomal compartments
183 (Engstler et al., 2004). Following HRP/ferritin endocytosis, the cells were fixed and embedded
184 in Epon resin. To visualize HRP, photooxidation with 3,3'-diaminobenzidine (DAB) was
185 employed before acquiring tomographic data (Figure 1 A, B, and D). Analysis of the
186 reconstructed electron tomograms of various BSF cells revealed a morphologically intricate
187 system of endosomes comprised of interconnected and fenestrated membrane networks. The
188 main endosome, spanning the posterior region of the cell from the vicinity of the flagellar
189 pocket (FP) to the Golgi apparatus, exhibited elongated (Figure 1 A and B) and circular
190 membrane sheets (Figure 1 C and D), encompassing a volume with a diameter of approximately
191 2 µm and a length of 4 µm. The localization of endosomes was strictly confined to the posterior
192 cytoplasm. Their precise positioning, however, appeared to be flexible, indicating a lack of
193 direct and rigid connection with the microtubule cytoskeleton. This observation is not
194 surprising, as there are no reports of cytoplasmic microtubules in trypanosomes. All
195 microtubules appear to be either subpellicular or within the flagellum. However, it is very
196 likely that a scaffold is necessary to maintain the intricate membrane structure of the endosomal
197 system, especially given the constant deformation of the cell body by the beating of the attached
198 flagellum. The electron tomograms further suggest that the large size of the endosomes may
199 render them unable to pass through the space between the nucleus and pellicular microtubules.
200 Another notable finding was the proximity of endosomes to the Golgi apparatus (Figure 1 A
201 and B), suggesting a potential involvement of the endosomal system in post-Golgi transport.

202 To investigate potential negative impacts of processing steps (cargo uptake, centrifugation,
203 washing) on endosomal organization, we directly fixed cells in the cell culture flask, embedded
204 them in Epon, and conducted electron tomography. The resulting tomograms revealed
205 endosomal organization consistent with that observed in cells fixed after processing (see
206 Supplementary movie 2, 3, and 4).

207 In summary, electron tomography analyses provided evidence that the endosomal system in
208 BSF cells is a complex, flexible, and largely continuous membrane network.

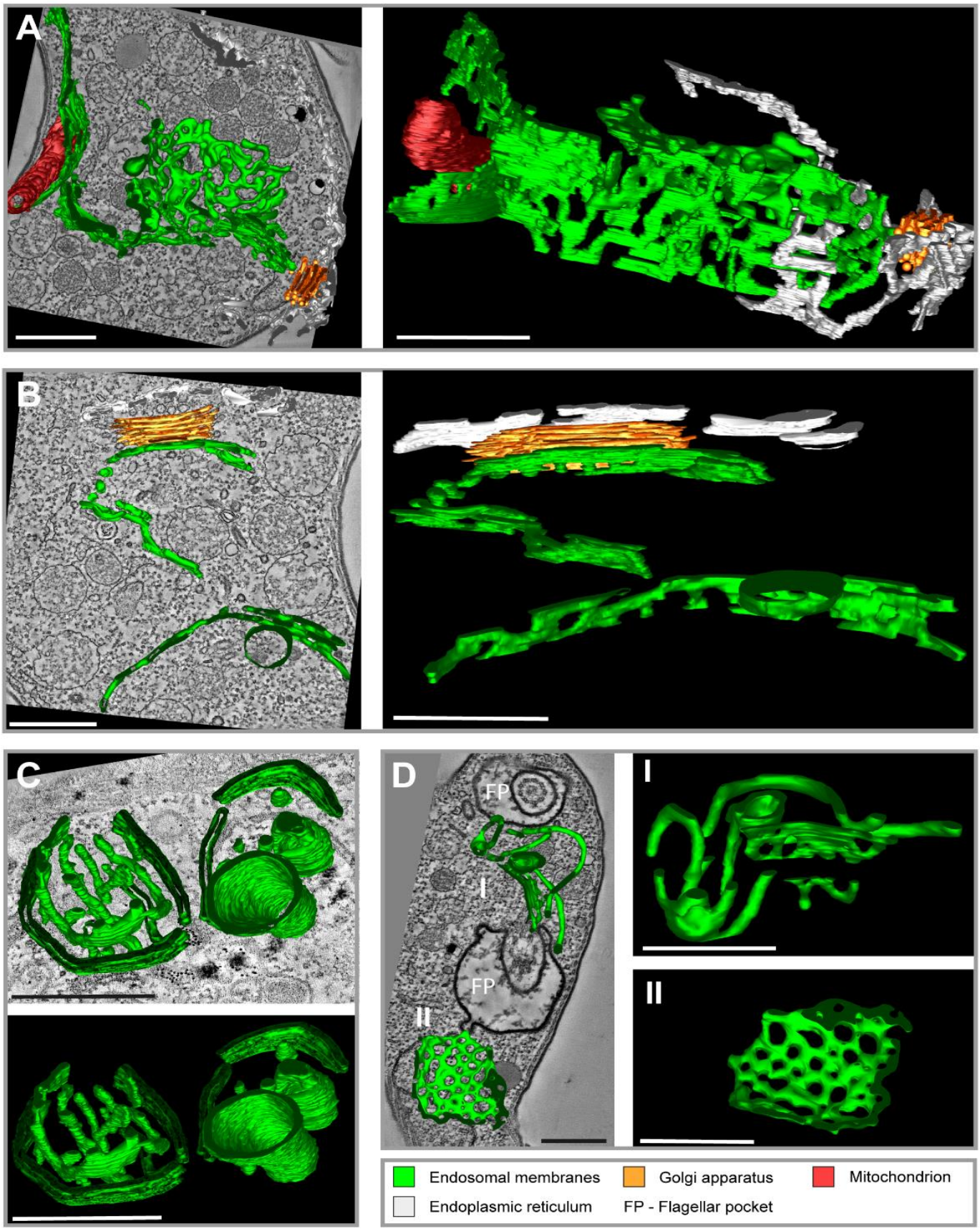
A
B
C
D
FP
I
FP
II
I
II
Endosomal membranes
Golgi apparatus
Mitochondrion
Endoplasmic reticulum
FP - Flagellar pocket

209

210

211 **Figure 1. Tomographic reconstructions of the endosomal apparatus of *T. brucei* after cargo uptake reveals**
212 **a large and mostly continuous membrane system. (A)** Elongated and highly fenestrated endosomal sheets and
213 palisades. **(B)** Elongated and slightly fenestrated endosomes. **(C)** Large circular endosomal cisternae. **(D)** Two
214 different substructures are displayed: one contains tubular palisades (I) while the other one is a heavily
215 fenestrated sheet (II). HRP endocytosis and DAB photooxidation were performed prior to tomogram acquisition
216 (A, B and D). Ferritin endocytosis was performed prior to tomogram acquisition (C). All sections are 250 nm
217 thick. The reconstructions (A) and (D) are based on three and two sections, respectively. The reconstructions (C)
218 and (D) are based on one section each. The section and corresponding tomogram (C) originate from the same
219 sample block as the image in Figure 4 I from Engstler et al. (2004). Endosomal membranes are shown in green.
220 The endoplasmic reticulum is visualised in white colour. The Golgi apparatus is labelled in orange and the
221 mitochondrion is shown in red. Abbreviation: flagellar pocket (FP). Scale bars: 500 nm. Movies corresponding
222 to panel A-D can be found here: A) z-stack, 3D model; B) z-stack, 3D model; C) z-stack, 3D model; D) z-stack,
223 3D model. The tomograms provided serve as a representative sample among the 37 tomograms that were
224 recorded.
225
226
227
228
229
230
231
232
233
234
235
236
237
238

239 **Super-resolution microscopy reveals the endosomal apparatus as a largely continuous**
240 **structure**

241 To be able to do specific labelling of the endosomal compartment, we first tested the potential
242 of various super-resolution light microscopy techniques to resolve and corroborate the structure
243 of the entire endosomal compartment (Figure 2 and S1). To allow the identification of
244 endosomes, we utilized the marker protein EP1 that had previously been demonstrated to label
245 the entire endosome and flagellar pocket of bloodstream form trypanosomes (Engstler and
246 Boshart, 2004). EP1, a cell surface protein found in insect stage trypanosomes, is mostly
247 excluded from the VSG coat of bloodstream form (BSF) trypanosomes.

248 To utilize EP1 as an endosomal membrane marker in *direct* stochastic optical reconstruction
249 microscopy (*d*STORM) (Heilemann et al., 2008), an EP1::HaloTag expressing cell line was
250 generated (Figure S2). The transgenic parasites were then labelled with a HaloTag ligand
251 conjugated to Alexa Fluor™ 647 (custom conjugated, see Methods), and imaged in 100 mM
252 MEA photo-switching buffer (Figure S1).

253 As expected, the EP1::HaloTag signal was localized in the posterior region of the cell, between
254 the nucleus and kinetoplast (Figure S1, I – II). Although the entire endosomal compartment
255 seemed to be labelled and gave the appearance of a largely connected system (Figure S1, III –
256 IV), the labelling density was not consistently strong, resulting in occasionally thin membrane
257 bridges (Figure S1, upper row, image IV, indicated by an arrow). In addition, the 3D volume
258 of the labelled region was too large (approx. 4 x 4 x 5 µm) to be completely captured by single-
259 molecule localization microscopy. On top of that, not all cells exhibited an EP1::Halo signal,
260 indicating heterogeneous gene expression within the population (Figure S1, lower row, lower
261 cell).

262 To overcome the non-uniform labelling density based on an endogenous marker protein and to
263 be able to capture the entire 3D volume of the parasite, a combination of dextran uptake assays
264 and expansion microscopy (Chen et al., 2015) was performed to visualize the endosomes. The
265 fluorescently labelled dextran was observed in the posterior region between the nucleus and
266 kinetoplast in all cells (Figure 2 A). The expanded and unexpanded cells revealed elongated
267 cable-like structures representing the endosomes, spanning from the flagellar pocket to the
268 vicinity of the nucleus. The expansion process improved the resolution of the structure,
269 allowing for the visualization of potential circular cisternae (Figure 2 A, middle row, image III,
270 arrow). While the flagellar pocket labelling was visible in nearly all unexpanded cells, not all

271 expanded cells exhibited a corresponding signal (Figure 2 A). To improve the resolution even
272 further, we performed structured illumination microscopy (SIM) on expanded cells (Figure
273 2 B). The result also demonstrated a largely continuous dextran signal between the nucleus and
274 the kinetoplast, indicating the continuity of the endosomal structures.

275 To determine the expansion factor, the diameter of the flagellar pocket and the length of the
276 endosomes were measured in multiple expanded and unexpanded cells (Figure 2 C). The
277 median diameter of the fluorescence signal corresponding to the flagellar pocket increased from
278 0.84 µm to 3.08 µm, resulting in an expansion factor of 3.6. The median length of the
279 endosomes increased from 2.51 µm to 7.88 µm, yielding an expansion factor of 3.1.

280 In summary, super-resolution microscopy using a transgenic marker cell line and cargo uptake
281 assays supported the possibility that in trypanosomes endosomes are largely continuous.

282

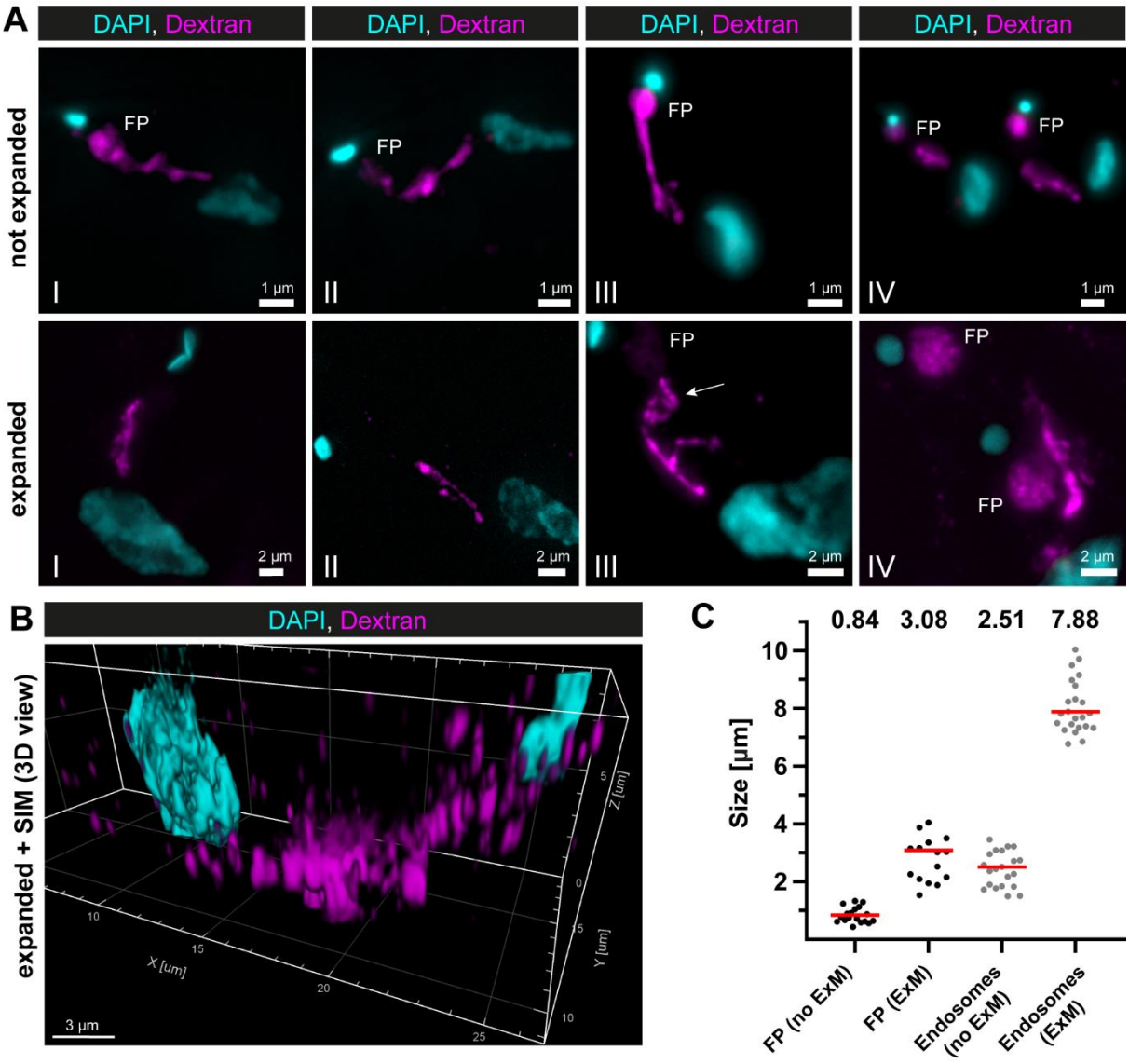

Figure 2. Super-resolution light microscopy reveals continuous endosomal membranes. (A) Visualisation of the endosomal system in *T. brucei* using expansion microscopy. Bloodstream form cells were pulsed with dextran conjugated to Alexa488 and fixed with 4 % formaldehyde and 0.2 % glutaraldehyde. Shown are exemplary images (I – IV) of not expanded and expanded cells imaged using widefield microscopy. All images represent a merge of DAPI staining (cyan) and dextran signal (magenta). Flagellar pockets (FP) are annotated. **(B)** 3D presentation of the endosomal system using a combination of expansion microscopy and structured illumination microscopy (SIM). The same gels as imaged in (B) were analysed with SIM. The 3D presentation was generated using the IMARIS package (Bitplane). **(C)** Scatter plot of the quantification of the expansion factor. The diameter of the fluorescence signal corresponding to flagellar pocket (FP) and length of the endosomes were measured in multiple not expanded (no ExM) and expanded cells (ExM) ($n \geq 15$). The median values are indicated as red bars and the corresponding numbers are shown in the upper part of the panel.

298 **Quantitative 3D colocalization analysis reveals overlaps between early, late and recycling**
299 **endosomal marker proteins**

300 To functionally characterize different components of the endosomal system, specific antibodies
301 against the endosomal marker proteins TbRab5A (early endosomes), TbRab7 (late endosomes),
302 and TbRab11 (recycling endosomes) were generated and validated (Figure S3).
303 Immunofluorescence assays were conducted, and the samples were imaged using 3D widefield
304 microscopy. For quantitative colocalization analyses the previously established endosomal
305 marker EP1::GFP (Engstler and Boshart, 2004) was used to define the entire endosomal
306 compartment as the region of interest (ROI) (Figure 3).

307 The EP1::GFP fluorescence revealed a variable number of high intensity signals, surrounded,
308 and connected by weaker signals (Figure 3 A, I). The fluorescence of the TbRab marker proteins
309 was present in foci of varying numbers, sizes, and intensities (Figure 3 A, II – IV). The
310 fluorescence signals for all three marker proteins were within the ROI defined by EP1. The
311 visualization as maximum intensity projections (MIP) suggested that the different subdomains
312 exhibited a low degree of colocalization and could represent physically distinct compartments
313 for early, late, and recycling endosomes (Figure 3 A, V). To quantitate this finding, 3D objects
314 were generated from the fluorescent signals for colocalization analysis using IMARIS (Figure
315 3 A, VI – X). These objects showed areas of unique staining as well as partially overlapping
316 regions. The pairwise colocalization of different endosomal markers is shown in Figure 3 A,
317 XI - XIII and 3 B. The different cells in Figure 3 B were chosen to represent the dynamic nature
318 of the labelled structures. Consequently, the selected cells provide diverse examples of how the
319 labelling can appear.

320 For the colocalization analysis, the EP1::GFP objects were masked and used as a 3D ROI in
321 IMARIS. The colocalization matrix (Figure 3 C) showed that TbRab5A and TbRab7 exhibited
322 the highest signal overlap, with approximately 53 % volume in both combinations. While 35 %
323 of the volume of TbRab5A was colocalized with TbRab11, 26.5 % of the volume of TbRab11
324 was colocalized with TbRab5A. The differences in colocalization volumes can be attributed to
325 the larger volume of the TbRab11 positive compartment. Similar observations were made for
326 the combination of TbRab7 and TbRab11. While 45 % of the volume of TbRab7 was
327 colocalized with TbRab11, 29.9 % of the volume of TbRab11 was colocalized with TbRab7.
328 Furthermore, the different marker combinations yielded comparable moderate correlation
329 coefficients (Pearson) ranging from 0.37 (TbRab5A and TbRab11) to 0.43 (TbRab5A and
330 TbRab7) (Figure 3 D).

In summary, the quantitative colocalization analyses revealed that on the one hand, the endosomal system features a high degree of connectivity, with considerable overlap of endosomal marker regions, and on the other hand, TbRab5A, TbRab7, and TbRab11 also demarcate separated regions in that system. These results can be interpreted as evidence of a continuous endosomal membrane system harbouring functional subdomains, with a limited amount of potentially separated early, late or recycling endosomes.

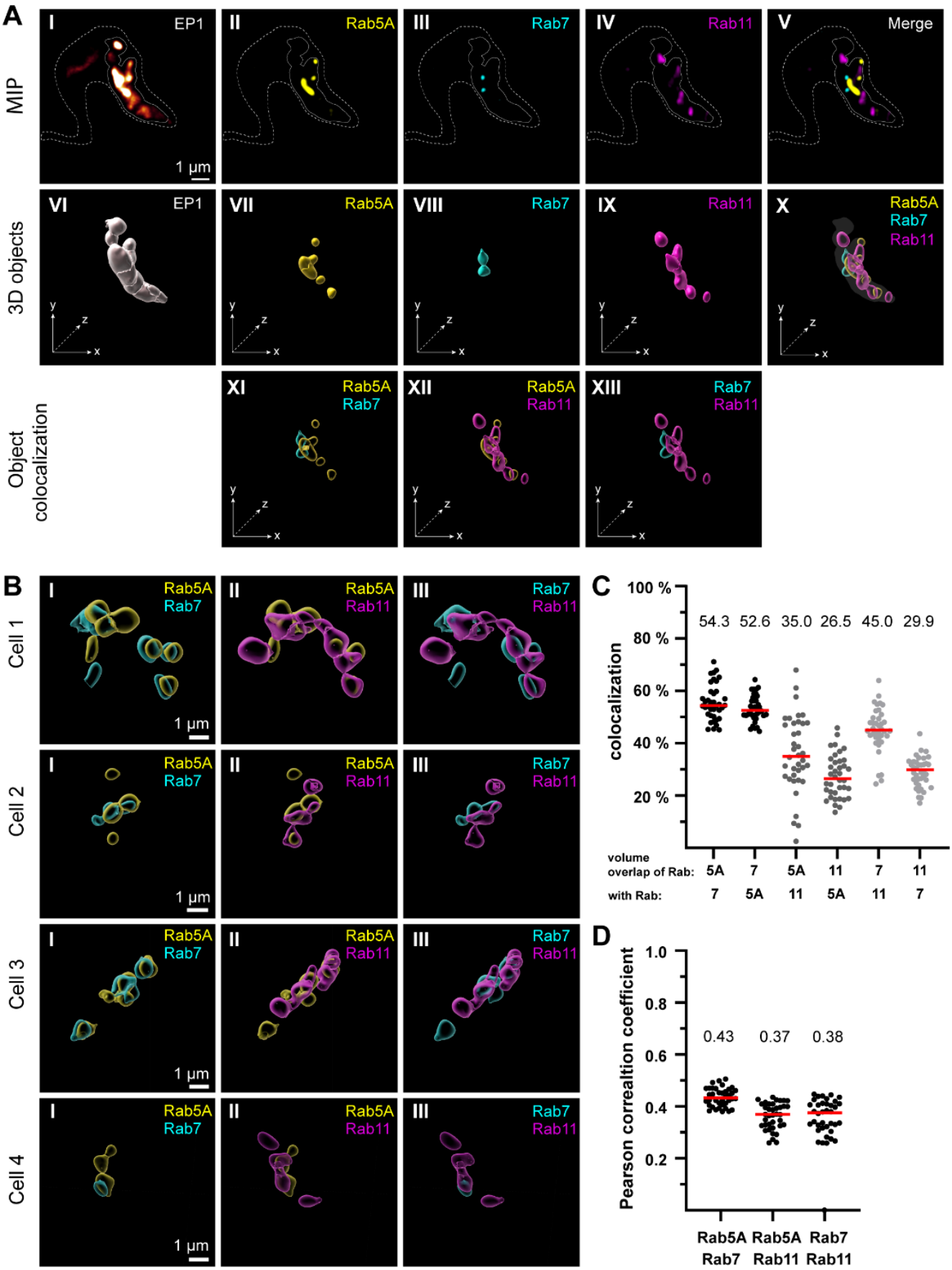
A
MIP
3D objects
Object colocalization
I EP1
II Rab5A
III Rab7
IV Rab11
V Merge
1 µm
VI EP1
VII Rab5A
VIII Rab7
IX Rab11
X Rab5A Rab7 Rab11
XI Rab5A Rab7
XII Rab5A Rab11
XIII Rab7 Rab11
B
Cell 1
Cell 2
Cell 3
Cell 4
C
colocalization
100 %
80 %
60 %
40 %
20 %
54.3 52.6 35.0 26.5 45.0 29.9
volume overlap of Rab: 5A 7 5A 11 7 11
with Rab: 7 5A 11 5A 11 7
D
Pearson correaltion coefficient
1.0
0.8
0.6
0.4
0.2
0.43 0.37 0.38
Rab5A Rab7
Rab5A Rab11
Rab7 Rab11

357

358

359 **Figure 3. The endosomal markers TbRab5A, TbRab7, and TbRab11 partly colocalize in the posterior**
360 **region of the cell. (A)** The experimental workflow, from fluorescence images to object generation and quantitative
361 3D colocalization analysis, is exemplified. EP1::GFP (I) expressing cells were fixed and labelled with anti-
362 TbRab5A (II), anti-TbRab7 (III) and anti-TbRab11 (IV) antibodies and imaged using widefield microscopy. Upper
363 row: maximum intensity projections (MIP) for each individual fluorescence channel (I – IV) as well as a merge of
364 all three anti-TbRab marker channels (V). The outline of the cell is shown by a dashed line (I - V) and the region
365 of interest (endosomal system) is presented by a solid line (I - V). Middle row: Corresponding 3D objects to display
366 the region of interest (VI) and the TbRab marker objects (VII – IX). The merge of all objects confirmed that the
367 TbRab marker objects are located within the region of interest (X). Lower row: Colocalization of the objects
368 representing TbRab5A and TbRab7 (XI), TbRab5A and TbRab11 (XII), TbRab7 and TbRab11 (XIII). The x-, y-
369 and z-axes are indicated to support the three-dimensional view. **(B)** Object colocalization shown for additional
370 cells. The colocalization of TbRab5A and TbRab7 (I), TbRab5A and TbRab11 (II), and TbRab7 and TbRab11
371 (III) is shown for different cells. (Cells 1 – 4). **(C - D)** Quantification of colocalization analysis for TbRab marker
372 combinations. The colocalization function of IMARIS was used for the quantification. The EP1 surfaces defined
373 the ROI (see panel A) and the automatic thresholding function (Costes et al., 2004) ensured minimal user bias.
374 Each data point (n = 38) represents a field of view with 30 – 40 cells, corresponding to a total number of ~ 1,200
375 analysed cells. The median is highlighted with a red line and the corresponding number is written on top of the
376 dataset. **(C)** Scatter plot of the colocalization analysis for the different TbRab marker combinations using the
377 percentage of volume overlap. **(D)** Scatter plot of the colocalization analysis for the different TbRab marker
378 combinations using the Pearson correlation coefficient.

379

380

381

382

383

384

385

386

387

388

389

390

391 **The endosomal markers TbRab5A, TbRab7 and TbRab11 are present on the same**
392 **membranes**

393 To investigate the potential functional sub-compartmentalization of endosomes in
394 trypanosomes, we conducted immunogold assays on Tokuyasu cryosections. We defined gold
395 particles that were 30 nm or closer to a membrane as membrane-bound, considering a
396 conservative calculation where two IgG molecules, each 15 nm in size, are positioned between
397 the bound epitope and the gold particle (Figure 4, panel A). Consequently, gold particles located
398 further away may represent cytoplasmic TbRab proteins or, as the "linkage error" can also occur
399 in the z-plane, correspond to membranes that are not visible within the 55 nm thickness of the
400 cryosection (Figure 4, panel C, arrows). The immuno-labelled structures exhibited a range of
401 architectural features, including vesicular and tubular cisternae with circular or elongated
402 shapes (Figure 4, 5, 6). The tubular structures had a thickness of 20 – 30 nm and extended up
403 to a few microns in length (with the longest example shown in Figure 5, panel F, arrow).
404 Vesicular shapes were observed in various sizes ranging from 30 nm to 135 nm in diameter.

405 While there were endosomal structures exclusively labelled with TbRab5A or TbRab7 (Figure
406 4 D, E, and G), a significant number of endosomal structures were labelled with both marker
407 proteins (Figure 4, B - G). In contrast to TbRab5A and TbRab7, TbRab11 tended to form signal
408 clusters on elongated structures (Figure 5 A, B, and D; Figure 6 D - F). TbRab11 was observed
409 together with TbRab5A (Figure 5 A - F) or TbRab7 (Figure 6 A - G) on the same endosomal
410 membranes, but it was also found as the sole marker on other endosomal membranes (Figure 5
411 B, D, F; Figure 6 C and G). The structures with a disk shape and positive for TbRab11 (Figure
412 5 F) were identified as exocytic carriers, as previously described in Grünfelder et al. (2003).
413 Another noteworthy observation was that long elongated structures tended to have no or only
414 weak labelling with any of the TbRab markers (Figure 5, panel F, arrow). To exclude potential
415 artifacts, both gold size combinations were utilized for all marker combinations.

416 In summary, the exemplary images shown in Figures 4, 5 and 6 demonstrate the colocalization
417 of TbRab5A, TbRab7 and TbRab11 on the same membranes, suggesting that the endosomal
418 membrane system is unlikely to consist of distinct and independent compartments for early, late
419 and recycling endosomes.

420

421

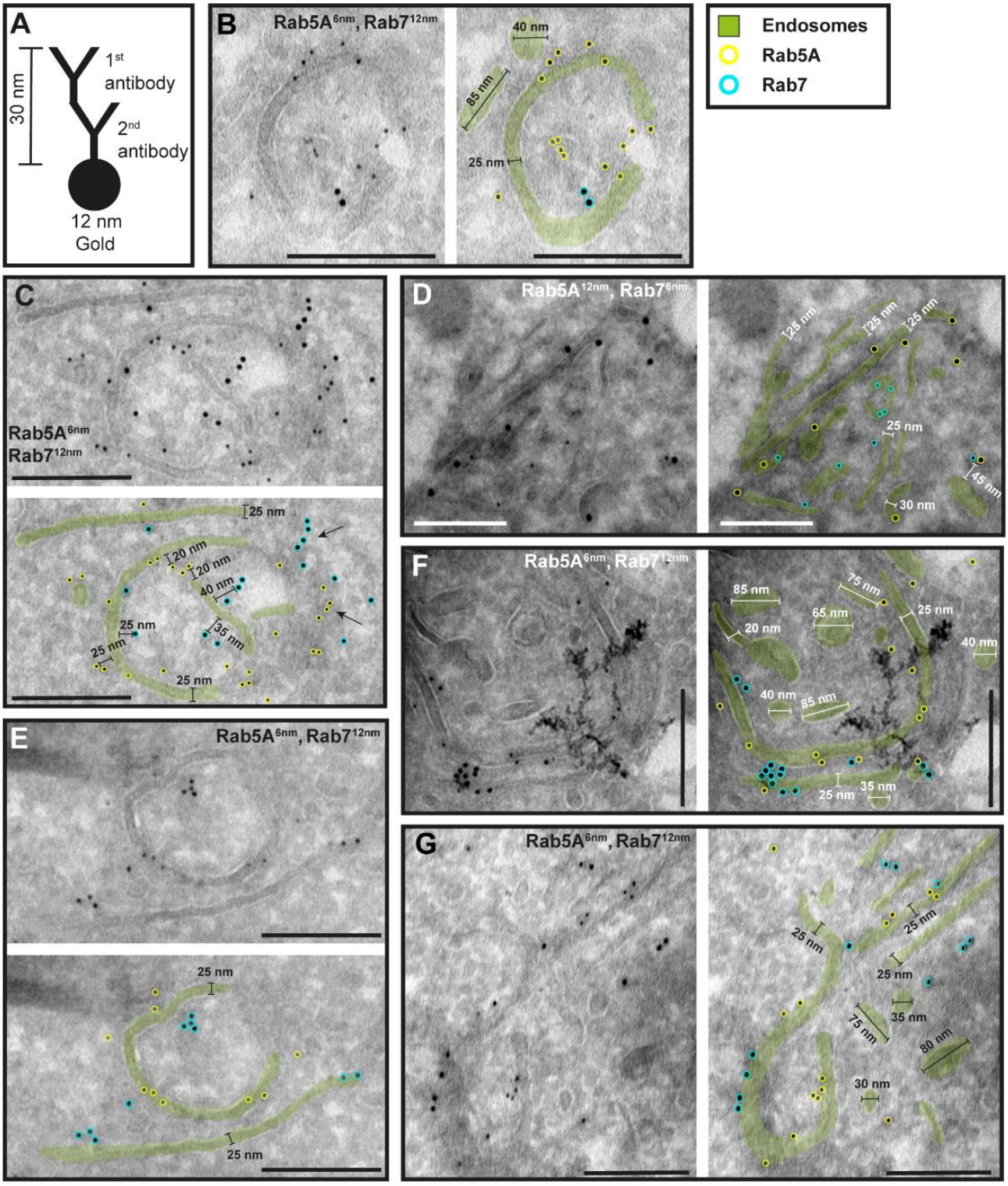

Figure 4. The endosomal markers TbRab5A and TbRab7 are present on the same membrane. (A) Schematic representation of antibody binding to visualise the maximum linkage error of 30 nm between a bound epitope and the gold particle. **(B - G)** Electron micrographs of cryosections labelled with rat anti-TbRab5A and guinea pig anti-TbRab7 antibodies and visualized with 6 or 12 nm gold-coupled secondary antibodies. For each panel an annotated and an unedited version of the image is presented. Endosomes are highlighted in green. Gold particles corresponding to TbRab5A signals are labelled in yellow. Gold particles corresponding to TbRab7 signals are highlighted in cyan. Scale bars: 200 nm. The images shown are representative examples drawn from over 300 micrographs generated in four distinct labelling experiments.

430

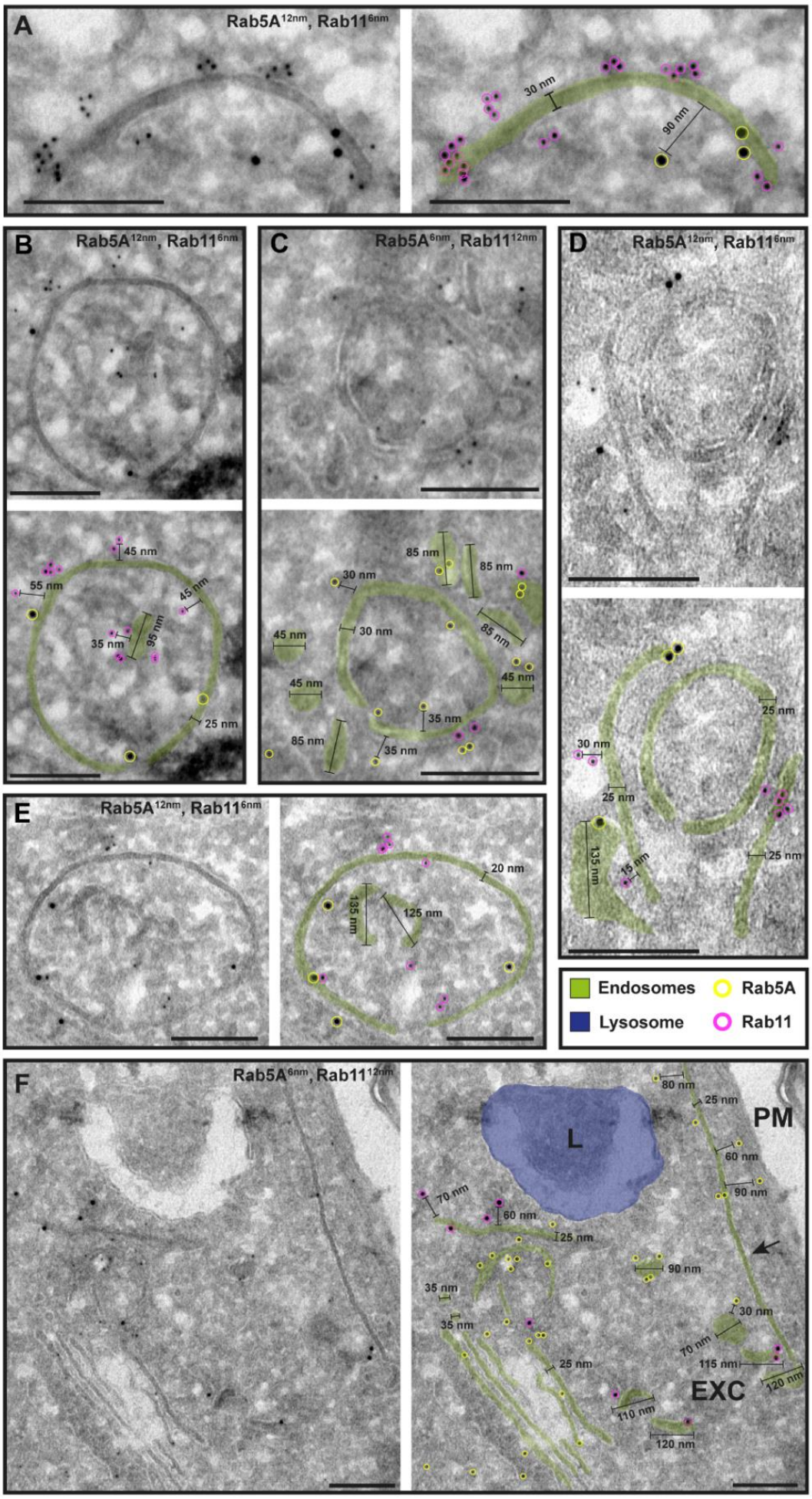
A
Rab5A12nm, Rab116nm
30 nm
90 nm
B
Rab5A12nm, Rab116nm
45 nm
55 nm
45 nm
35 nm
95 nm
25 nm
C
Rab5A6nm, Rab1112nm
85 nm
85 nm
30 nm
45 nm
30 nm
85 nm
45 nm
45 nm
35 nm
85 nm
35 nm
D
Rab5A12nm, Rab116nm
25 nm
30 nm
25 nm
135 nm
15 nm
25 nm
E
Rab5A12nm, Rab116nm
20 nm
135 nm
125 nm
Endosomes
Rab5A
Lysosome
Rab11
F
Rab5A6nm, Rab1112nm
80 nm
25 nm
PM
L
60 nm
90 nm
70 nm
60 nm
25 nm
90 nm
35 nm
30 nm
35 nm
70 nm
25 nm
115 nm
120 nm
EXC
110 nm
120 nm

Figure 5. The endosomal markers TbRab5A and TbRab11 are present on the same membranes. (A - F) Electron micrographs of cryosections labelled with rat anti-TbRab5A and rabbit anti-TbRab11 antibodies and visualized with 6 or 12 nm gold-coupled secondary antibodies. For each panel an annotated and an unedited version of the image is presented. Endosomes are marked in green, and the lysosome is highlighted in blue. Gold particles are marked in yellow (TbRab5A) and in magenta (TbRab11). Scale bars: 200 nm. Exocytic carrier (EXC), lysosome (L), plasma membrane (PM). The displayed images are representative examples drawn from over 300 images generated in four distinct labelling experiments.

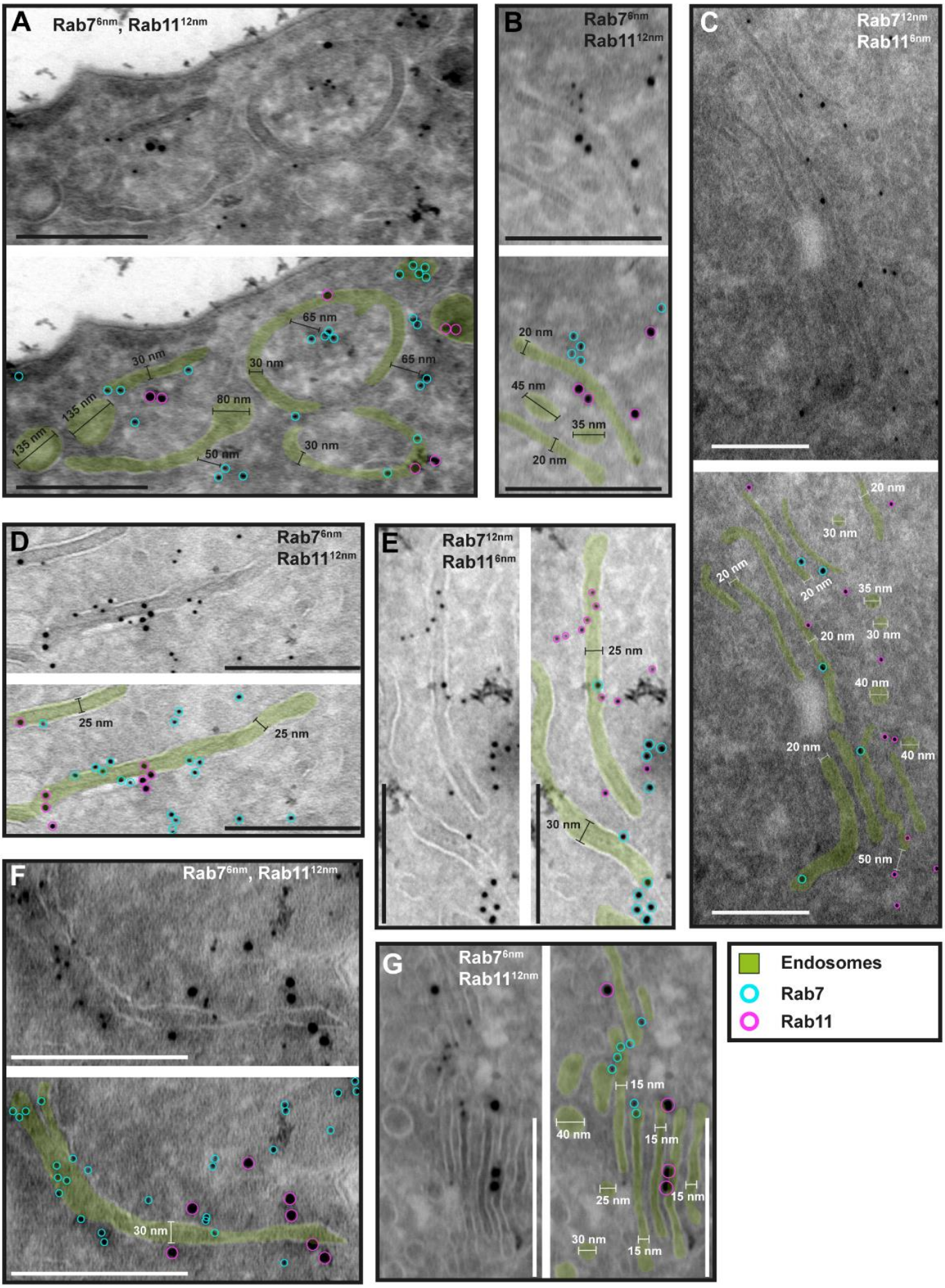
A
Rab7 6nm, Rab11 12nm
65 nm
30 nm
30 nm
65 nm
135 nm
135 nm
80 nm
50 nm
30 nm
B
Rab7 6nm
Rab11 12nm
20 nm
45 nm
35 nm
20 nm
C
Rab7 12nm
Rab11 6nm
20 nm
30 nm
20 nm
20 nm
35 nm
20 nm
30 nm
40 nm
20 nm
40 nm
50 nm
D
Rab7 6nm
Rab11 12nm
25 nm
25 nm
E
Rab7 12nm
Rab11 6nm
25 nm
30 nm
F
Rab7 6nm, Rab11 12nm
30 nm
G
Rab7 6nm
Rab11 12nm
15 nm
40 nm
15 nm
25 nm
15 nm
30 nm
15 nm
Endosomes
Rab7
Rab11

Figure 6. The endosomal markers TbRab7 and TbRab11 are present on the same membranes. (A - G) Electron micrographs of cryosections labelled with guinea pig anti-TbRab7 and rabbit anti-TbRab11 antibodies visualized with 6 or 12 nm gold-coupled secondary antibodies. For each panel an annotated and an unedited version of the image is presented. Endosomes are highlighted in green. Gold particles are labelled in cyan (TbRab7) and in magenta (TbRab11). Scale bars: 200 nm. The displayed images are representative examples drawn from over 200 images generated in three distinct labelling experiments.

To confirm that the analysed membrane structures indeed represent endosomal membranes, we conducted cargo uptake assays and anti-VSG immunogold labelling (Figure 7). Trypanosomes were either pulsed with fluid-phase cargo (BSA; Figure 7, A - C) or cargo was taken up by receptor-mediated endocytosis (transferrin, Tf; Figure 7, D - F), and the sections were subsequently labelled with anti-TbRab antibodies. BSA and transferrin perfused the entire endosomal system, with the conjugated 5 nm gold particles visible inside the endosomal structures (Figure 7, A - F). Moreover, gold particles were observed within vesicles (Figure 7, B and D) and accumulated within the lysosome (Figure 7, A and B). In another set of experiments, the parasites were not pulsed with cargo markers, but the sections were labelled with anti-VSG and anti-TbRab antibodies (Figure 7, G - I). The anti-VSG antibodies decorated the entire plasma membrane (Figure 7, G) as well as intracellular membrane structures (Figure 7, G - I). The different TbRab marker proteins were found on the same membrane structures as the cargo markers or the anti-VSG antibodies (Figure 7, all panels). In summary, the use of cargo markers and antibodies targeting VSG and endosomal marker proteins confirmed the identity of the trypanosome endosomes.

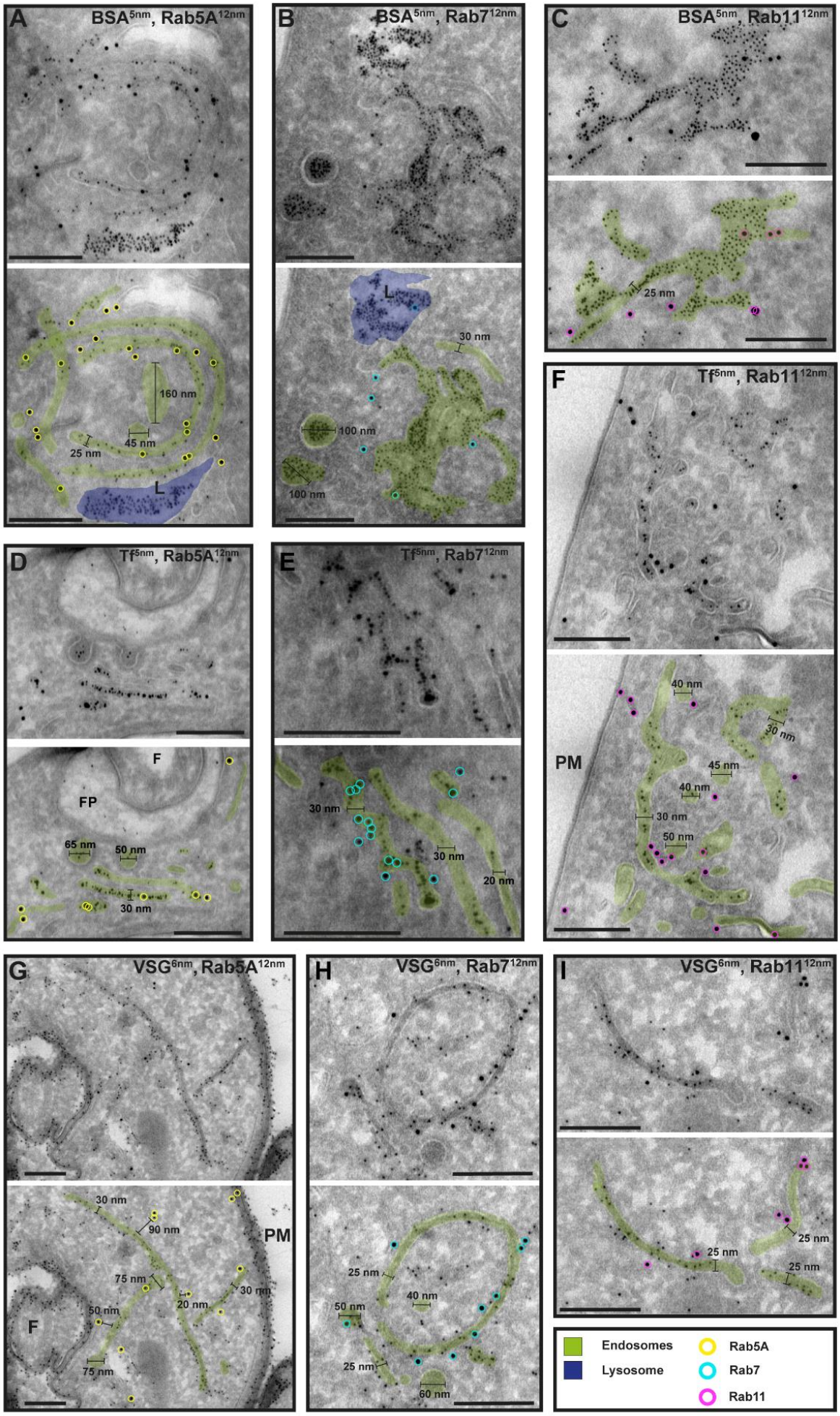
A
BSA5nm, Rab5A12nm
160 nm
45 nm
25 nm
L
B
BSA5nm, Rab7 12nm
L
30 nm
100 nm
100 nm
C
BSA5nm, Rab11 12nm
25 nm
D
Tf5nm, Rab5A 12nm
F
FP
65 nm
50 nm
30 nm
E
Tf5nm, Rab7 12nm
30 nm
30 nm
20 nm
F
Tf5nm, Rab11 12nm
40 nm
30 nm
PM
45 nm
40 nm
30 nm
50 nm
G
VSG6nm, Rab5A 12nm
30 nm
90 nm
PM
75 nm
30 nm
20 nm
50 nm
F
75 nm
H
VSG6nm, Rab7 12nm
25 nm
40 nm
50 nm
25 nm
60 nm
I
VSG6nm, Rab11 12nm
25 nm
25 nm
25 nm
Endosomes
Lysosome
Rab5A
Rab7
Rab11

525 **Figure 7. Cargo uptake and anti-VSG immunogold labelling confirm the endosomal identity. (A – I)** Electron
526 micrographs of cryosections labelled with anti-TbRab5A (yellow), anti-TbRab7 (cyan) or anti-TbRab11 (magenta)
527 antibodies and 12 nm gold-conjugated secondary antibodies. For each panel an annotated and an unedited version
528 of the image is presented. Endosomes are highlighted in green, the lysosome in blue. Parasites were incubated with
529 5 nm gold-conjugated BSA **(A – C)** or transferrin (Tf) **(D – F),** prior to fixation, sectioning and immunolabelling.
530 BSA and transferrin cargo was observed in vesicles, endosomes, and lysosome. **(H – I)** Cells were labelled with
531 anti-VSG antibodies and 6 nm gold-conjugated secondary antibodies. (F), flagellum, (FP) flagellar pocket, (PM)
532 plasma membrane, (L) lysosome. Scale bars: 200 nm. The displayed images are representative examples drawn
533 from over 50 images generated in three distinct labelling experiments.

534

535

536

537

538

539

540

541

542

543

544

545

546

547

548

549

550

551

552

553 **3D Tokuyasu demonstrates that trypanosomes have continuous endosomal membranes**

554 Following the visualization of continuous endosomal membranes through cargo uptake assays
555 in Epon resin sections (Figure 1), we aimed to confirm these findings using 3D immuno-
556 electron microscopy on cryosections (Figure 8). Cryosections with a thickness of 250 nm were
557 labelled with antibodies against TbRab5A, TbRab7, and TbRab11. The 3D reconstructions
558 provided an in-depth view of the interconnected circular and tube-like structures. Although the
559 tomograms represented only a 250 nm thick section of a cell, it was evident that the membrane
560 system likely exhibited further connections above and below the field of view. This assumption
561 was confirmed by our experiments with conventional electron tomography. The 3D Tokuyasu
562 method effectively highlighted the interconnectedness of these structures, expanding upon the
563 observations from 2D analyses. Interestingly, these tomograms did not exhibit the fenestration
564 pattern identified in traditional electron tomography. We suspect that this is due to
565 methodological reasons. The Tokuyasu procedure uses only aldehydes to fix all structures.
566 Consequently, effective fixation of lipids occurs only through their association with membrane
567 proteins. Thus, the lack of visible fenestration is likely due to possible loss of lipids during
568 incomplete fixation.

569 We observed endosomes decorated with different TbRab signals, supporting our assumption
570 that functional subdomains exist within the same endosomal membrane system (Figure 8, A II
571 and III, B II). It is worth noting that smaller gold particles demonstrated better penetration of
572 the cryosections, explaining the higher abundance of 6 nm gold particles compared to 12 nm
573 gold particles. Another noteworthy finding was the presence of TbRab5A and TbRab7 in the
574 lysosomal lumen, suggesting their possible degradation (Figure 8, A and B).

575 In addition, the endosomal membranes were juxtaposed to the trans-Golgi in all Tokuyasu
576 tomograms, further implying a role of the endosomal system in post-Golgi trafficking (Figure
577 8, A I and B III). In summary, our second 3D electron microscopy approach successfully
578 visualized the continuous membrane system of the endosomal apparatus in *T. brucei* and
579 represents the first utilization of the advanced 3D Tokuyasu technique in trypanosomes.

580

581

582

583

584

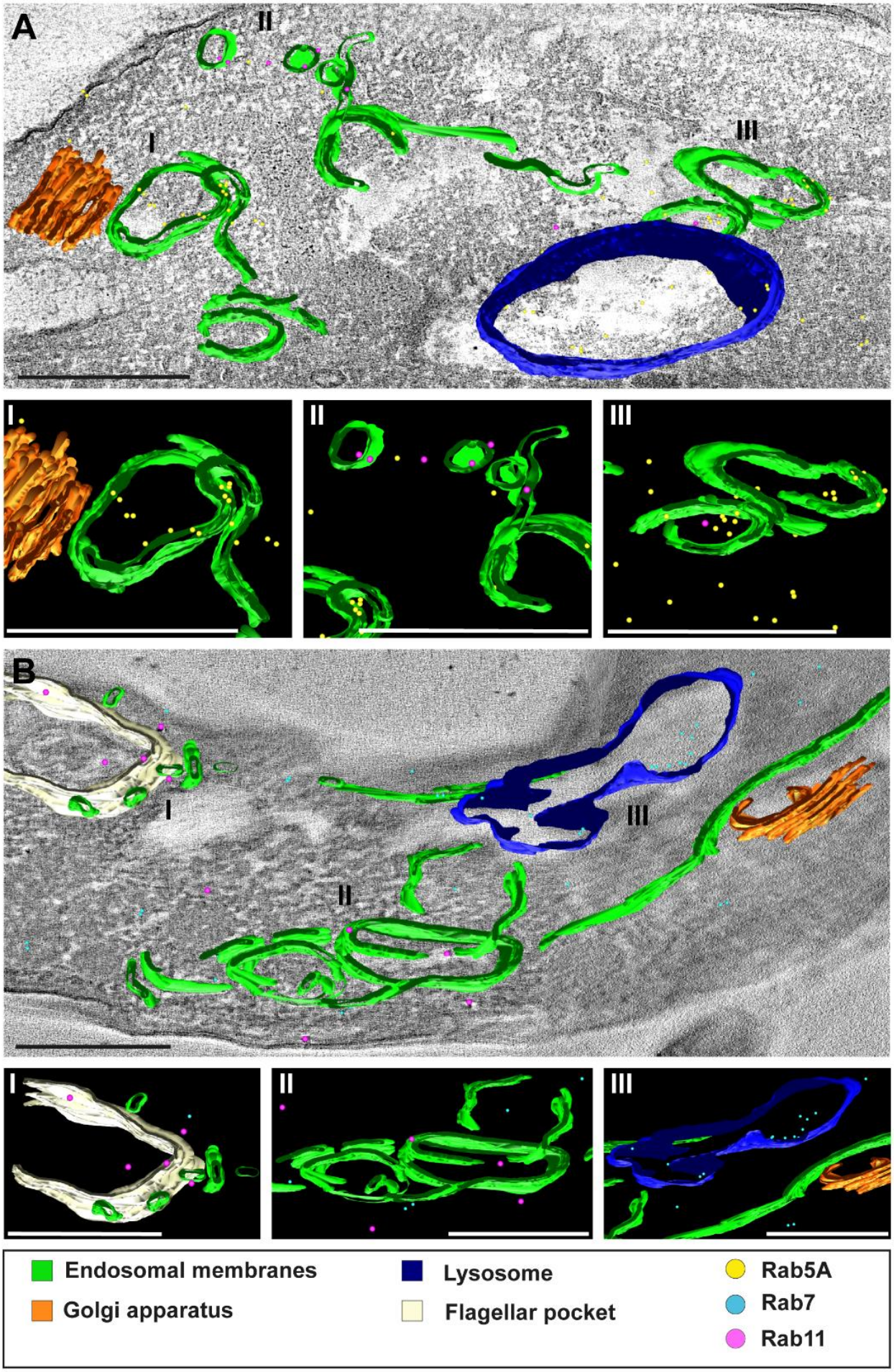
A
I
II
III
B
I
II
III
Endosomal membranes
Golgi apparatus
Lysosome
Flagellar pocket
Rab5A
Rab7
Rab11

585 **Figure 8. 3D Tokuyasu demonstrated continuous endosomal membranes in cryosections. (A, B)**
586 Tomographic reconstruction of the endosomal apparatus. **(I – III)** Isolated view of different organelle structures.
587 Cryosections (250 nm) were labelled with anti-TbRab antibodies and 6 or 12 nm gold-coupled secondary
588 antibodies. Endosomes are shown in green, lysosomes in blue, the flagellar pocket in white, the Golgi apparatus
589 in orange. Gold particles are indicated as coloured spheres; TbRab5A (yellow), TbRab7 (cyan) or TbRab11
590 (magenta). Scale bars: 500 nm. Movies corresponding to panel A and B can be found here: A) z-stack, 3D model;
591 B) z-stack, 3D model. The provided tomograms serve as a representative sample among the 35 tomograms that
592 were recorded.

593

594

595

596

597

598

599

600

601

602

603

604

605

606

607

608

609

610

611 ## Discussion

612 Evolution has endowed African trypanosomes with a cellular multi-tool, the VSG-surface coat.
613 Apart from exhibiting antigenic variation across hundreds of coat variants, the VSG proteins
614 are attached to the cell surface through GPI-moieties, enabling their remarkable mobility.
615 Exploiting this feature, the parasites evade early immune responses by clearing antibodies. This
616 evasion process hinges upon the highly polarized nature of the trypanosome cell body, with
617 exclusive endocytic uptake occurring at the posterior end, coupled with an exceptionally rapid
618 membrane recycling rate. The prevailing model of the endosomal system, consisting of distinct
619 compartments for early, late, and recycling endosomes, seems incompatible with the observed
620 rapid turnover rates in *T. brucei*. Nevertheless, the parasite expresses the canonical Rab
621 GTPases which serve as markers for these endosomal compartments, such as Rab5 (early),
622 Rab7 (late), and Rab11 (recycling endosomes). To resolve this apparent contradiction, we
623 performed a structure-function analysis of the trypanosome endosome apparatus.

624 3D electron tomography reconstructions, utilizing cargo uptake assays (Figure 1;
625 Supplementary movie 1), revealed a complex network of endosomal structures in *T. brucei*.
626 These compartments were characterized by interconnected fenestrated sheets, circular
627 cisternae, and tubular structures, that formed a single intricate endosome. Our results shine a
628 new light on transmission electron microscopic studies of the trypanosome endomembrane
629 system (reviewed in Link et al., 2021). Based on 2D information the giant endosomal sheets
630 had been interpreted as extended tubular structures, fenestrations as vesicles and the connective
631 areas as irregularly shaped structures (Engstler et al., 2004; Grünfelder et al., 2003; Overath
632 and Engstler, 2004).

633 In mammalian cells, tubular endosomes constitute a major part of the endosomal system.
634 Tubules possess a higher surface area-to-volume ratio compared to vacuolar regions. As a
635 result, they have been proposed to geometrically sort membrane-associated proteins over
636 soluble cargo (Mayor et al., 1993). It is assumed that the carrier tubules, following detachment,
637 transport their cargo either to the plasma membrane or to the recycling endosomes.

638 *T. brucei* lacks elongated tubulo-vesicular structures. Furthermore, our tomographic analysis
639 did not reveal the conventional tubular carriers (reviewed in Chi et al., 2015). Instead, in these
640 parasites, geometric sorting most likely occurs at the rims of flat, fenestrated sheets. A specific
641 class of clathrin-coated vesicles (CCV II) pinches off from these strongly curved membrane

642 areas. They transport bulky fluid phase cargo and membrane protein complexes (such as
643 VSG^{IgG}) to the lysosome (Engstler et al., 2004; Grünfelder et al., 2003).

644 The sorting mechanism into CCV II vesicles could be a purely physical process. Both the
645 fenestrated sheets and circular cisternae exhibit the same inner width of about 35 nm. The VSG
646 coat occupies 2 x 15 nm of this width, significantly limiting the available volume for fluid phase
647 cargo. As the VSG concentration in the membrane increases, the bulky cargo is pushed towards
648 the edges of the sheets, resulting in further membrane deformation that facilitates the
649 recruitment of clathrin. The VSG is excluded from the CCV II and thus not transported to the
650 lysosome. How this works mechanistically is unknown, however, it is tempting to speculate
651 that the geometric sorting of larger cargo into the CCV II, sterically excludes VSG.

652 The electron tomographic analysis of the *T. brucei* endosome yielded compelling evidence of
653 an extensive and interconnected membrane system. While this conclusion is supported by a
654 substantial number of tomograms, the technique is not well suited for quantitative analyses.

655 Therefore, we conducted super-resolution microscopy and cargo uptake assays (Figure 2 and
656 S1). To analyse the full 3D volume of the cell, expansion microscopy was conducted (Figure
657 2). The visualised endosomal network looked like the elongated and circular structures found
658 in the reconstruction of the electron tomograms (Figure 1). While the elongated structures could
659 easily correspond to the fenestrated sheets (Figure 2 A), the circular structure (Figure 2 A,
660 middle row, image III, arrow) nicely recapitulates the morphology of a circular cisternae
661 (Figure 1 C). Interestingly, dividing cells (possessing two kinetoplasts and two flagellar
662 pockets) always showed a fluorescence signal corresponding to the endosomal system
663 juxtaposed only to the "old" flagellar pocket, indicating that the duplication of the endosomal
664 network might occur *de novo* during the cell cycle. This is currently speculation and requires
665 more in-depth analysis. The 3D presentation (Figure 2 B) confirmed the continuity of the
666 endosomal membranes, which had been seen already in the electron tomography.

667 In contrast to *d*STORM or SIM, expansion microscopy (ExM) offers a selective perspective on
668 the trypanosome endosomal system. To date, ExM has been effectively employed to visualize
669 cell structures associated with the cytoskeleton or other stabilizing supports (Alonso, 2022;
670 Amodeo et al., 2021; Gambarotto et al., 2019; Gorilak et al., 2021; Kalichava and Ochsenreiter,
671 2021). However, we could not find any published ExM images of endosomes. Our initial efforts
672 to identify endosomal markers using ExM were also unsuccessful. Only when we added the

673 inert fluid phase cargo dextran did the endosomes become clearly visible. This was likely due
674 to the stabilizing effect of the cargo.

675 Having established that the endosomes in trypanosomes likely form a continuous cellular
676 structure, our next inquiry was whether this would be evident in the simultaneous presence of
677 the canonical marker proteins TbRab5A, TbRab7, and TbRab11. To define the region of interest
678 in 3D immunofluorescence microscopy, we utilized the previously established fluorescent
679 marker EP1::GFP (Engstler and Boshart, 2004), which stains the entire endosomal system.
680 Maximum intensity projections (MIPs) of multichannel images indicated that the TbRabs were
681 closely juxtaposed but in distinct endosomal compartments (Figure 3 A, upper row). This
682 finding aligns with the results of a previously published quantitative colocalization analysis of
683 TbRab5A and TbRab7 (Engstler et al., 2004). However, the presentation as 3D objects already
684 implied an overlap between the different marker proteins. The present study now reveals that
685 endosomal sheets can easily span over several micrometres, which fundamentally alters the
686 interpretation of the light microscopy colocalization data. Thus, the seemingly separate
687 structures could well be subdomains of the same membrane structure.

688 We therefore performed quantitative colocalization analyses with all marker combinations
689 (Figure 3). The degree of colocalization was assessed by determining the percentage of overlap
690 for the volume of one TbRab marker colocalized with another. Notably, TbRab5A and TbRab7
691 exhibited a significantly higher percentage of overlap (about 53 %) compared to the other
692 marker combinations (Figure 3 C). An overlap of Rab5 and Rab7 has also been found in
693 mammalian cells where it has been attributed to a temporary phenomenon during the maturation
694 of early to late endosomes (Podinovskaia et al., 2021; Rink et al., 2005; van der Beek et al.,
695 2021).

696 Interestingly, TbRab7 exhibited a higher degree of colocalization with TbRab11 (45 %) than
697 TbRab5A showed with TbRab11 (35 %). This observation could indicate a functional
698 polarization within the flagellar pocket. TbRab11 is known to decorate disk-shaped structures
699 called exocytic carriers (EXCs), which transport the recycled VSG coat back to the cell surface.
700 Boehm and colleagues (2017) report that in the flagellar pocket endocytic and exocytic sites
701 are in close proximity but do not overlap. We further suggest that the fusion of EXCs with the
702 flagellar pocket membrane and clathrin-mediated endocytosis take place on different sites of
703 the pocket. This disparity explains the lower colocalization between TbRab11 and TbRab5A.
704 It is worth noting that the mechanism by which Golgi-derived membrane and cargo are
705 transported to the flagellar pocket in trypanosomes remains unclear. In our view, the most

706 plausible scenario involves feeding into the rapid endocytic recycling pathway, which is further
707 supported by the absence of tubular carriers as observed in mammals.

708 Quantitative colocalization analysis by 3D IF provides statistically valid results, however, has
709 the obvious limitation that it lacks ultrastructural information. Therefore, we analysed the
710 localization of the different TbRab proteins on cryo-electron micrographs. This finally proved
711 that different TbRab markers can be found on the same membrane structures and argues against
712 the existence of distinct early, late, and recycling endosomal compartments in *T. brucei* (Figures
713 4, 5 and 6). An alternative explanation for the two marker proteins residing on the same
714 membrane would the endosome maturation model, which has been proposed in mammals
715 (Poteryaev et al., 2010; Rink et al., 2005; Stoorvogel et al., 1991). In short, early endosomes
716 undergo maturation and transform into late endosomes through a series of changes. This
717 maturation process involves the acquisition of new membrane proteins and enzymes that among
718 others facilitate a decrease in the pH value. Ultimately, the late endosomes fuse with lysosomes,
719 leading to cargo degradation (reviewed in Podinovskaia and Spang, 2018).

720 EM-cryosections provide high-resolution 2D information. To gain volume information, we
721 resorted to an extremely demanding technique that combines ultrastructural 3D information
722 with immunodetection. 3D Tokuyasu has not been applied to trypanosomes and the utilisation
723 of 3D immunogold has not been used on endosomes in any system. The Tokuyasu tomograms
724 clearly showed the connection of circular cisternae and sheet-like structures in 3D (Figure 8).
725 The decoration with different endosomal marker proteins demonstrated the existence of
726 functional subdomains within a giant endosomal membrane system convincingly, and finally
727 offered an explanation to the fundamental question of how trypanosomes can combine
728 endosomal functionality with very fast membrane recycling.

729 Our work has certainly raised more questions than it has answered. One puzzling aspect is the
730 presence of extended sheet-like endosomal structures that display sparse or no labelling of
731 TbRab proteins. This is particularly intriguing when considering the substantial membrane area
732 covered by these sheets. It is tempting to speculate that the absence of canonical markers
733 correlates with a lack of endosomal function. We postulate that these sheets represent
734 "endosomal highways" that support fast flow of cargo by facilitated diffusion. This may allow
735 for the efficient transport of VSG and fluid-phase cargo between distinct functional endosomal
736 subdomains, which can be in close proximity or at a distance of microns apart. Consequently,
737 the slow vesicular trafficking process in trypanosomes could be limited to clathrin-coated

738 vesicles, originating either from the flagellar pocket or the rims of fenestrated sheets and
739 cisternae, as well as to Rab11-positive exocytic carriers.

740 Interestingly, we did not find any structural evidence of vesicular retrograde transport to the
741 Golgi. Instead, the endosomal 'highways' extended throughout the posterior volume of the
742 trypanosomes approaching the trans-Golgi interface. It is highly plausible that this region
743 represents the convergence point where endocytic and biosynthetic membrane trafficking
744 pathways merge. A comparable merging of endocytic and biosynthetic functions has been
745 described for the TGN in plants. Different marker proteins for early and recycling endosomes
746 were shown to be associated and/ or partially colocalized with the TGN suggesting its function
747 in both secretory and endocytic pathways (reviewed in Minamino and Ueda, 2019). As we could
748 not find structural evidence for the existence of a TGN we tentatively propose that
749 trypanosomes may have shifted the central orchestrating function of the TGN as a sorting hub
750 at the crossroads of biosynthetic and recycling pathways to the endosome. Although this is a
751 speculative scenario, it is experimentally testable.

752 In summary, we confirmed the endosomal identity of the analysed membranes with the aid of
753 cargo uptake assays (Figure 1, 2 and 7), transgenic cell lines (Figure 2 and 3) as well as immuno
754 labelling (Figure 3 - 8) combined with various light and electron microscopy methods. In the
755 process, we ensured that all examined membranes belonged to the endosomal system and we
756 did not, for example, mischaracterize ER membranes as endosomal membranes. All our results
757 suggest that the endosomal apparatus consists of a continuous membrane system with
758 TbRab5A, TbRab7 or TbRab11 positive subdomains that can be dynamically formed (Figure
759 9). Thus, the overall architecture of the trypanosome endosomes represents an adaptation that
760 has facilitated the extreme speed of plasma membrane recycling observed in these organisms.

761 A partially continuous endosomal membrane structure has been proposed in the South
762 American parasite *Trypanosoma cruzi* (Alcantara et al., 2018; Porto-Carreiro et al., 2000),
763 however, no endosome markers were used in that study to corroborate their findings. In the
764 single-celled parasite *Giardia*, the peripheral vesicles that constitute the endosomal organelles
765 form an "interconnected network" (reviewed in Benchimol and de Souza, 2022), while the
766 endosome-like compartment in *Toxoplasma* is likely involved in both endocytic and exocytic
767 trafficking (reviewed in McGovern et al., 2021). In *Leishmania,* the endosomal system has not
768 been fully characterized but seems to be under physical tension (reviewed in Ansari et al.,
769 2022). Thus, parasitic protozoa might feature interesting variations of the common cell
770 biological process of endocytosis. Furthermore, these variations might extend to many other

organisms beyond the extensively studied, yet not entirely representative model organisms. The emergence of technologies such as CRISPR and single-cell analyses now enables the systematic exploration of the vast diversity of eukaryotic cells. Therefore, the systematic investigation of the phylogeny of cell biological inventions could be a logical next step.

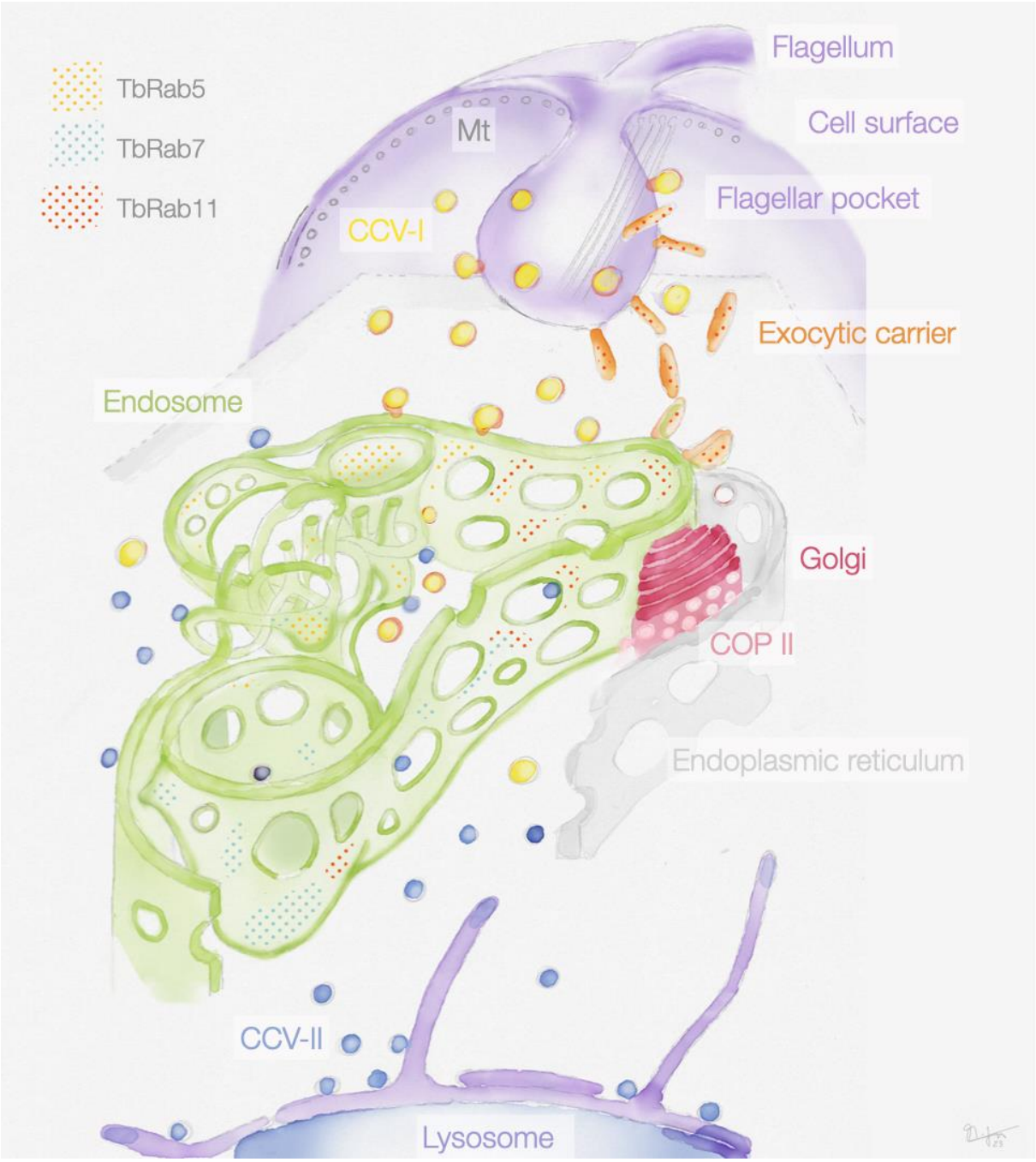

Figure 9. Schematic representation of the endosomal system in *T. brucei*. The endosome is marked by the presence of small GTPases of the Rab family: Rab5A (yellow dots), Rab7 (cyan dots), and Rab11 (red dots). Class I clathrin-coated vesicles (CCV-I), class II clathrin-coated vesicles (CCV-II), vesicles coated with coat protein (COP) II.

842 # Material and methods

843 **Cell culture and cell lines**

844 *T. brucei* bloodstream-form parasites (Lister strain 427, antigenic type MITat 1.2, clone 221)
845 were cultured in HMI-9 medium (Hirumi and Hirumi, 1989) supplemented with 10 % heat-
846 inactivated foetal calf serum (Sigma-Aldrich), 100 U/ml penicillin and 0.1 mg/ml streptomycin.
847 The cells were maintained at 37 °C and 5 % CO_2 split at regular intervals to keep the population
848 densities below 1 x 10^6 cells/ml. Population density was monitored using a Z2 Coulter Counter
849 (Beckman Coulter). The monomorphic "13-90" parasites expressing the T7 RNA polymerase
850 and tetracycline repressor were cultivated in the presence of 5 µg/ml hygromycin and 2.5 µg/ml
851 G418 (Wirtz et al., 1999). The transgenic bloodstream form "2T1" cells which constitutively
852 express a T7 RNA polymerase and tetracycline repressor were cultivated in the presence of 2.5
853 µg/ml phleomycin and 1 µg/ml puromycin (Alsford et al., 2005). The RNAi cell lines (RNAi-
854 TbRab5A, RNAi-TbRab7, RNAi-TbRab11) were based on the 2T1 cell line and cultivated in
855 the presence of 5 µg/ml hygromycin and 2.5 µg/ml phleomycin. The transgenic EP1::GFP cells
856 were based on MITat1.2 expressing wild type cells and cultivated in the presence of 5 µg/ml
857 hygromycin and 15 µg/ml G418 (Engstler and Boshart, 2004). The transgenic single marker
858 (SM) cell line (Wirtz et al., 1999) which constitutively express a T7 RNA polymerase and
859 tetracycline repressor were cultivated in the presence of 2.5 µg/ml G418. The EP1::Halo tagged
860 cell line was based on SM cells and was cultivated in the presence of 2.5 µg/ml phleomycin and
861 2.5 µg/ml G418.

862

863 **Generation of RNAi cell lines**

864 The RNAi target sequences were selected by entering the target gene ORF into the RNAit
865 webapp (Redmond et al., 2003). The selected primer pairs flanked the base pairs 29 – 614
866 (TbRab5A), 134 – 630 (TbRab7) or 67 – 496 (TbRab11) and encoded the attB-sequence at the
867 5' end for the ligation into the pGL2084 plasmid (Jones et al., 2014). The plasmids were
868 linearized with AscI and 10 µg were transfected into 3 x 10^7 mid-log phase bloodstream 2T1
869 cells (Alsford et al., 2005) using Amaxa Basic Parasite Nucleofector Solution 1 using the X-001
870 program of an Amaxa Nucleofector II (Lonza, Switzerland). Clones were selected by growth
871 in medium containing phleomycin (2.5 µg/ml) and hygromycin (5 µg/ml).

872

873

874

875 **Generation of EP1::Halo cell line**

876 The insert for the EP1::HaloTag cell lines was generated in resemblance to the GFP::EP1 cell
877 line from Engstler and Boshart (2004). For this, the Halo tag was inserted in between the N-
878 terminal EP1 globular domain and the C-terminal EP1 stalk domain. The three fragments (EP1
879 globular domain, Halotag, EP1 stalk domain) were amplified using PCR. For the EP1
880 fragments, the GFP::EP1 plasmid was used (Engstler and Boshart, 2004). While amplifying the
881 globular domain, an internal BamHI restriction site was removed by silent point mutation. The
882 Halo tag sequence was amplified from the pFC20A (HaloTag®) T7 SP6 Flexi® vector
883 (Promega, USA). All amplified fragments were then combined using Gibson assembly (Gibson
884 assembly cloning kit, NEB) with 20 base pair overhangs. This construct was cloned into
885 pJet1.2blunt and later excised using HindIII and BamHI for ligation into the pLew100v5
886 expression vector (Wirtz et al., 1999). For transfection of the parental, SM cell line, 10 µg of
887 the NotI linearized plasmid was transfected. Clones were selected by growth in medium
888 containing phleomycin (2.5 µg/ml) and G418 (2.5 µg/ml). Primers used: forward primer
889 globular domain (AGTAAAATTCACAAGCTTGG
890 ATGGCACCTCGTTCCCTTTATCTGCTCGCTGTTCTTCTGTTCAGCGCGAACCTCTTC
891 GCTGGCGTGGGATTTGCCGCAGCCGCTGAAGGACCAGAAGACA), reverse primer
892 globular domain (CCGATTTCTGCCAT
893 TCTAGAGGTGGCGACCGGCCGGTGAATCCCGCCGACCTTGGTTCCCTTCTCGCCTT
894 TGCCTTTGCCTCCCTTAGTAAGACCCTTGTCTTCTGGTCCTTCAGCGGCT), forward
895 primer Halo tag, (TCTAGA ATGGCAGAAATCGGTACTGGCTTTCCATTCG), reverse
896 primer Halo tag (TCAGTGCCATTGGTATCGTCCTTAATT
897 AACCCGGAAATCTCCAGAGTAGACAGCC), forward primer stalk domain (TTAATTAA
898 G GACGATACCAATGGCACTGACC), reverse primer stalk domain
899 (AAAAGCCAACTAAATGGGCA GGATCC TTAGAATGCGGCAACGAGAGC).

900

901 **Growth curves**

902 Cells were seeded with a starting concentration below 1 x 10^6 cells/ml in a volume of 10 ml and
903 divided into two 2 ml aliquots in separate wells of a 24-well plate. Tetracycline was added to a
904 final concentration of 1 µg/ml in one well to induce RNAi or EP1::Halo expression. The
905 population density of the non-induced and induced cells was determined every 24 h over a time
906 course of 96 h, using a Z2 Coulter Counter (Beckman Coulter). Depletion of the target protein
907 was confirmed by immunoblotting of whole-cell lysates (Supplements 2).

908

909 **Cargo uptake**

910 Per assay the same number of cells (1 x 10^7 for light microscopy, 1 x 10^8 for electron
911 microscopy) were harvested by centrifugation (1500 x *g*, 10 min, 4 °C). After that, cells were
912 washed with 1 ml TDB (5 mM KCl, 80 mM NaCl, 1mM $MgSO_4$, 20 mM Na_2HPO_4, 2 mM
913 NaH_2PO_4, 20 mM glucose, pH 7.6), harvested by centrifugation (1500 x *g*, 2 min, 4 °C) and the
914 supernatant was discarded. Next, the cells were resuspended in 100 µl TDB and incubated with
915 either dextran-Alexa488 (light microscopy), transferrin-gold conjugates or BSA-gold
916 conjugates (electron microscopy) for 15 min at 37 °C or HRP/ferritin for 5 min at 37 °C
917 (electron microscopy). The final concentration of both dextran (ThermoFisher cat. number:
918 D22910) and HRP (horseradish peroxidase type II, Sigma) was 10 mg/ml. The final
919 concentration of ferritin (horse spleen ferritin, type I, Sigma) was 50 mg/ml. Transferrin-gold
920 (Cytodiagnostics) or BSA-gold (Alexa555-BSA-Au, UMC Utrecht) were added to a final
921 OD = 5. The uptake reactions were stopped by adding 1 ml of the corresponding fixatives (4 %
922 formaldehyde and 0.2 % glutaraldehyde for the dextran uptake, 2 % formaldehyde and 0.2 %
923 glutaraldehyde for BSA and transferrin uptake, 2.5 % glutaraldehyde for HRP uptake, 2 %
924 formaldehyde and 1 % glutaraldehyde for ferritin uptake). Cells were fixed for 20 min on ice
925 followed by 30 min at RT (for dextran uptake), 1 hour at RT (for HRP and ferritin) or 2 hours
926 at RT (for BSA and transferrin uptake). Following this, cells were treated either as described in
927 the immunofluorescence section or as explained in the sample embedding and immuno-electron
928 microscopy section.

929

930 **EP1::Halo cell labelling**

931 Cells were harvested (1400 x *g*, 10 min, 37 °C) and washed in 1 ml TDB. The cell pellet was
932 resuspended in 100 µl fresh TDB and HaloTag ligand (either in-house labelled Alexa647 ligand
933 or Halo-Tetramethylrhodamine (TMR, Promega, USA) was added to a final concentration of
934 500 nM (Alexa647) or 5 nM (TMR). The labelling reaction was performed for 15 min at 37 °C
935 and stopped by the addition of 4 % formaldehyde in PBS.

936

937 **Immunofluorescence**

938 Cells were harvested (1400 x *g*, 10 min, 37 °C), washed in ice-cold TDB, and fixed with 4%
939 formaldehyde overnight (4 °C) or for 1 hour at RT. Fixed samples were washed in 1 ml PBS,
940 harvested (1400 x *g*, 90 sec, RT) and 1 x 10^6 cells were added to each Ø 12 mm coverslip coated
941 with 0.01 % poly-L-lysine (> 20 min, RT). The cells were attached to the coverslips by

942 centrifugation (750 x *g*, 1 min, RT) and attachment was confirmed visually. The attached cells
943 were then permeabilized in 0.25 % Triton X-100 in PBS (5 min, RT) and blocked in 3 % (w/v)
944 BSA in PBS (30 min, RT). Sequentially, coverslips were incubated with primary antibodies (1
945 h, RT), washed with PBS (3 x 5 min), and incubated once more with secondary antibodies (1
946 h, RT, in the dark). Finally, samples were washed in PBS (3 x 5 min), rinsed in ddH_2O, carefully
947 dried, and mounted on glass slides using ProLong™ Diamond Antifade (Life Technologies).
948 Antibodies were diluted in 1 % (w/v) BSA in PBS as follows: rat anti-TbRab5A 1:250, guinea
949 pig anti-TbRab7 1:250, rabbit anti-TbRab11 1:250, goat anti-rat conjugated with Alexa Fluor
950 647 1:500, goat anti-guinea pig conjugated with CF568 1:500, goat anti-rabbit conjugated with
951 Alexa Fluor 405 1:500.
952

953 **Expansion microscopy**

954 The proExM method was performed as described in (Tillberg et al., 2016) with some
955 modifications. Approximately 1 x 10^7 cells were harvested by centrifugation (1500 x *g*, 10 min,
956 4 °C), then washed with 1 ml TDB, harvested by centrifugation (1500 x *g*, 2 min, 4 °C) again,
957 and the supernatant was discarded. Next, the cells were resuspended in 100 µl TDB and
958 incubated with dextran-Alexa488 for 15 min at 37 °C. The final concentration of dextran
959 (ThermoFisher cat. number: D22910) was 10 mg/ml. The reaction was stopped by adding 1 ml
960 4 % formaldehyde and 0.2 % glutaraldehyde in PBS. Cells were fixed for 20 min on ice
961 followed by 30 min at RT. After the fixation, cells were adhered to 12 mm coverslips. For
962 anchoring of proteins, a solution of 5 mg AcX (A20700, Invitrogen), dissolved in freshly
963 opened 500 µl anhydrous DMSO (D12345, Invitrogen), was prepared. A 100 µl drop of AcX
964 1:100 in PBS was placed on parafilm in a humidity chamber, the coverslips were inverted and
965 incubated at room temperature for 16 hours. Coverslips were returned to a 24-well plate, washed
966 twice for 5 minutes with PBS and stored in the fridge until the end of the day. For gelation,
967 gelling solution was made mixing 100 µl monomer solution with 0.5 µl 10 % (v/v) APS and
968 0.5 µl TEMED, vortexed and used straight away. A volume of 50 µl was placed on a piece of
969 parafilm in a humidity chamber and the coverslips were inverted and incubated at 37 °C for one
970 hour. Monomer solution was prepared with sodium acrylate 8.6 % (w/v) (408220, Sigma),
971 acrylamid 2.5 % (w/v), N-N'-methylenebisacrylamide 1.5 % (w/v) (M7279, Sigma) and NaCl
972 11.7 % (w/v) (AM9760G, Ambion) in PBS. Sodium acrylate stock solution 33 % (w/v) was
973 prepared by dissolving 1.9 g in 5 ml of ddH_2O, 0.2 mm-filtered and used freshly. After
974 polymerization, coverslips with the gel stuck to it were transferred to a 6-well plate with 1 ml
975 of digestion solution (0.5 % Triton X100, 1 mM EDTA, pH 8 (AM9260G, Ambion), 50 mM

976 Tris, pH 8 (AM9855G, Ambion) and 1 M NaCl (AM9760G, Ambion) freshly supplemented
977 with 10 U/ ml proteinase K (P8107S, New England Biolabs). Plates were slightly tilted to
978 ensure the coverslip was completely covered and incubated at room temperature overnight. The
979 next day, gels were detached from the coverslips and transferred to a Petri dish. After three
980 rounds of expansion with 20 ml ddH_2O for 30 minutes each, gels were mounted in a poly-D-
981 lysine coated imaging chamber (Nunc 155360 Lab-Tek II Chambered Coverglass with Cover,
982 No. 1.5 Borosilicate Sterile) and imaged using a DMi8 widefield microscope.
983

984 **Fluorescence microscopy**

985 Images were acquired using a DMi8 widefield microscope (Thunder Imager, Leica
986 Microsystems, Germany) with a HCX PL APO CS objective (100 x oil-immersion, NA 1.4,
987 working distance 90 µm) and Type F Immersion Oil (refractive index = 1.518, Leica
988 Microsystems, Germany). The microscope was operated using LAS-X software (Leica).
989 Samples were illuminated with an LED8 light source (Leica) and 50 % illumination power.
990 Excitation light was selected by using following filter sets: 391/32 nm; 479/33 nm; 554/24 nm;
991 638/31 nm (Leica Microsystems, Germany). Emitted light was collected at 435/30 nm (DAPI
992 and Alexa Fluor 405), 519/25 nm (Dextran-Alexa Fluor 488 and GFP), 594/32 nm (CF568 and
993 TMR) and 669 nm (Alexa Fluor 647), respectively. The individual exposure times were as
994 follows: DAPI, Alexa Fluor 405, CF568, Alexa Fluor 647 = 200 ms; GFP = 500 ms; Dextran-
995 Alexa Fluor 488 = 2 s; TMR = 2 s. Differential interference contrast (DIC) was used to visualise
996 cell morphology. 3D recording of each field of view was obtained using 48 z-slices (step size
997 = 0.21 µm). Fields of view were selected based on DIC to subjectively select for areas
998 containing enough cells and blind the user to the fluorescence signal of the protein markers of
999 interest. Images were captured using a Leica K5 sCMOS camera (pixel size 6.5 µm). The LAS-
1000 X/ Thunder integrated instant computational clearing (ICC) algorithm was used to remove
1001 background signal, using a minimal structure size of 338 nm.
1002

1003 **Colocalization analysis**

1004 Widefield microscopy images were deconvolved using Huygens Essential version 21.10
1005 (Scientific Volume Imaging B.V., Hilversum, Netherlands) and analyzed with IMARIS (9.9.1,
1006 Oxford Instruments). In brief, surfaces were rendered for the EP1 signal, and checked manually
1007 for accurate posterior localization in morphologically intact cells. These EP1 surfaces were used
1008 to define the ROI for colocalization analysis. The automatic thresholding function (Costes et

1009 al., 2004) was used to ensure objective thresholding for the colocalization analysis of the
1010 different TbRab marker protein combinations.
1011

1012 ***d*STORM imaging**

1013 Direct stochastic optical reconstruction (*d*STORM) imaging was performed on an inverted
1014 wide-field microscope (Olympus, IX-71). HaloTag-Ligand Alexa Fluor 647 was excited by a
1015 641 nm diode laser (Topica, iBeam smart 640-S), a 405 nm diode laser (Coherent, Cube 405-
1016 100C) was used for DAPI excitation. Both Lasers were spectrally cleaned with cleanup filters
1017 (Chroma, laser clean up filter 640/10 & 405/20) and focused on the back focal plane of a 60x
1018 oil-immersion objective (Olympus, 60x NA 1.45). Emission light was separated from excitation
1019 light using a dichroic beam splitter (Semrock, FF410/504/583/669) and further spectrally
1020 filtered by a long-pass filter (Semrock, 647 nm RazorEdge). Images were recorded on an EM-
1021 CCD camera chip (Andor, iXon DU-897) with a measured pixel size of 134 nm. *d*STORM
1022 imaging was performed in a buffer of 100 mM MEA (Sigma-Aldrich, #M6500) in PBS at pH
1023 7.4. Time series of 15 000 frames at an exposure time of 20 ms were captured while irradiating
1024 the sample by highly inclined laminated optical sheet (HILO) illumination with an intensity of
1025 approx. 2 kW cm^{-2}. Super-resolved images were reconstructed with rapidSTORM 3.3 (Wolter
1026 et al., 2012) and further processed for illustrations in Fiji. Widefield images of transmitted light
1027 and DAPI staining were captured after *d*STORM. For illustrations, the scale of the widefield
1028 images was matched to the super-resolved *d*STORM images.
1029

1030 **SIM imaging**

1031 Structured Illumination imaging was performed using a Zeiss Elyra 7 lattice SIM equipped with
1032 a 63x C-Apochromat 63x/1.20 W (Zeiss) water immersion objective, four excitation lasers
1033 (405 nm diode, 488 nm OPSL, 561 nm OPSL, and 642 nm diode laser) and two sCMOS (PCO,
1034 pco.edge 4.2) cameras. Four-fold expanded gels were transferred onto PDL coated single well
1035 chamber slides (CellVis, #C1-1.5H-N). For excitation of DAPI the 405 nm laser diode was set
1036 to 10 % output power, for excitation of Dextran-Alexa488 the 488 nm laser to 20 %. A
1037 respective exposure time of 100 ms and 200 ms was set for the two channels. Z-stacks were
1038 captured in 3D Leap mode with optimal step intervals and appropriate filter sets (BP 420-480
1039 + LP 655 and BP 495-550 + BP 570-620 for the DAPI- and 488-channel, respectively). SIM
1040 imaging was performed by capturing 13 phase-shifts of the lattice SIM pattern per slice. Super-

1041 resolved images are processed in ZEN 3.0 SR FP2 (black) (Zeiss, Version 16.0.10.306) with
1042 SIM and SIM² processing modules.
1043

1044 **Sample embedding and preparation for electron microscopy**

1045 For Tokuyasu immuno-EM, sample preparation and sectioning were performed as previously
1046 described (Engstler et al., 2004; Grünfelder et al., 2003; Möbius and Posthuma, 2019; Slot and
1047 Geuze, 2007). In short, 1 x 10^8 cells were harvested (1500 x *g*, 10 min, 37 °C) and washed with
1048 1 ml TDB. Cells were fixed by addition of 4 % formaldehyde and 0.4 % glutaraldehyde in 0.2
1049 M PHEM buffer (120 mM PIPES, 50 mM HEPES, 4 mM $MgCl_2$, 20 mM EGTA adjusted to
1050 pH 6.9 with 1 M NaOH) 1:1 to TDB. After 5 min the fixatives were replaced with 2 %
1051 formaldehyde and 0.2 % glutaraldehyde in 0.1 M PHEM for 2 hours at RT. Fixatives were
1052 removed by washing with 1 ml TDB and quenched with PBS + 0.15 % (w/v) glycine. Cells
1053 were pelleted and resuspended in 200 µl 12 % (w/v) gelatine (Rousselot 250 LP30) in 0.1 M
1054 PHEM at 37 °C and pelleted again. The pellets were solidified on ice, cut into smaller blocks,
1055 and infused with 2.3 M sucrose in 0.1 M PHEM overnight at 4 °C. The blocks were mounted
1056 on metal pins and stored in liquid nitrogen. The gelatine-embedded cells were cryosectioned to
1057 55 nm or 250 nm thick sections at -120 °C or -100 °C, respectively, with a DiATOME diamond
1058 knife in a Leica ultracut cryomicrotome (UC7). Sections were collected and deposited on
1059 formvar- and carbon-coated grids using 2.3 M sucrose and 1.8 % (v/v) methylcellulose (MC;
1060 Sigma M6385 25 centipoises) mixed 1:1.

1061 For Epon embedding, sample preparation and sectioning were performed as previously
1062 described (Langreth and Balber, 1975; Webster, 1989). In short, chemically fixed cells were
1063 pelleted (1500 x *g*, 10 min, RT) and washed 6 x in 0.12 M sucrose, 0.1 M cacodylate, pH 7.4.
1064 They were postfixed in 1 % (w/v) osmium tetroxide, stained *en bloc* in 1 % (w/v) uranyl acetate
1065 in 50 mM sodium maleate buffer (pH 5.1), dehydrated with ethanol and embedded at 60 °C in
1066 epoxy resin. Cells incubated with HRP were treated, in suspension, with diaminobenzidine
1067 (DAB) in 50 mM Tris-HCl (pH 7.6) containing 0.01 % (v/v) osmium tetroxide for 5 min prior
1068 to postfixation with 1 % osmium tetroxide. The epon-embedded cells were sectioned to 250 nm
1069 thick sections at RT.

1070

1071

1072

1073 **Immuno-electron microscopy**

1074 Grids with sections facing down were incubated in a 24-well plate with 2 ml PBS at 37 °C for
1075 30 – 60 min to remove gelatine, 2.3 M sucrose and 1.8 % MC mixture. Afterwards, the grids
1076 were washed on ~ 100 µl drops of PBS + 0.15 % (w/v) glycine and PBS on parafilm at RT (both
1077 3 x 5 min). The standard volume for all non-antibody related steps was100 µl. Next, blocking
1078 was performed in PBS + 0.1 % (v/v) acetylated BSA (BSA-c, Aurion) + 0.5 % (w/v) cold fish-
1079 skin gelatine (FSG, Sigma) for 30 min. The following primary antibody incubation was done
1080 for 1 – 2 hours in PBS + 0.1 % BSA-c + 0.5 % FSG. The used antibody dilutions were rat anti-
1081 TbRab5A 1:50, guinea pig anti-TbRab7 1:50, rabbit anti-TbRab11 1:25, and rabbit anti-VSG
1082 1:50. After that, grids were washed 5 x 5 min with PBS + 0.1 % BSA-c + 0.5 % FSG and
1083 incubated with corresponding gold coupled secondary antibodies for 1 – 2 hours (diluted 1:10
1084 in PBS + 0.1 % BSA-c + 0.5 % FSG). Further washing steps with PBS + 0.1 % BSA-c + 0.5 %
1085 FSG (3 x 5 min) and PBS (3 x 5 min) followed before all remaining antibodies were fixed with
1086 1.25 % glutaraldehyde for 5 min at RT. After three washing steps with ddH_2O to remove
1087 phosphate from the grids, sample contrast was increased by 5 min incubation on 2 % (w/v)
1088 uranyl acetate (UA) in water (pH 7) and 7 min incubation on 1.8 % (v/v) MC/ 0.3 % (w/v) UA
1089 in water (pH 4) (both on ice). Grids were retrieved with a metal ring and excess MC/UA was
1090 removed with filter paper. Grids were dried for at least 30 min at RT in the metal ring.

1091

1092 **Electron Microscopes**

1093 JEOL JEM-2100 transmission electron microscope (TEM) operated at 200 kV with camera
1094 system: TVIPS F416 4k x 4k.

1095 JEOL JEM-1400 Flash scanning transmission electron microscope (STEM) operated at 120 kV
1096 with camera system: Matataki Flash 2k x 2k.

1097 FEI Tecnai TF30 transmission electron microscope (TEM) operated at 300kV with camera
1098 system: Gatan US4000 4k x 4k CCD.

1099 The software Serial EM was used for tilt series acquisitions of electron tomograms. The
1100 subsequent reconstruction and segmentation were done using the IMOD software package
1101 (Kremer et al., 1996). For 2D electron micrographs pseudo colouring and highlighting was done
1102 using Adobe Illustrator 2022.

1103

1104

1105 **Immunoblotting**

1106 Trypanosomes were resuspended and lysed in protein sample buffer (60 mM Tris-HCl, pH 6.8,
1107 2 % (w/v) SDS, 10 % (v/v) glycerol, 0.002 % (w/v) bromophenol blue, 1 % (v/v)
1108 β-mercaptoethanol) to yield equivalents of 2 x 10^5 cells/µl. For quantification of TbRab proteins
1109 by Western Blot 20 µl of the protein sample was resolved on 12.5 % SDS-PAGE gels and
1110 transferred onto nitrocellulose membrane. The membranes were blocked for 1 h at room
1111 temperature with 5 % (w/v) milk powder in PBS. Next, the membranes were incubated in
1112 polyclonal primary antibodies diluted in PBS containing 1 % (w/v) powdered milk and 0.1 %
1113 (v/v) Tween 20, anti-TbRab 1:5000 and monoclonal mouse anti-TbPFR (L13D6) 1:20 (Kohl et
1114 al., 1999). After wash steps, the membranes were incubated in IRDye 800 CW (Li-Cor) labelled
1115 either goat anti-rat, donkey anti-guinea pig, or donkey anti-rabbit and IRDye 680 LT (Li-Cor)
1116 labelled goat anti-mouse secondary antibodies diluted 1:10,000 in PBS containing 1 % (w/v)
1117 milk powder and 0.1 % (v/v) Tween 20. Images were acquired and quantified with the Li-Cor
1118 Odyssey system.

1119

1120 **Recombinant protein expression and purification for antibody generation**

1121 The TbRab5A (Tb927.10.12960), TbRab7 (Tb927.9.11000), TbRab11 (Tb927.8.4330) open
1122 reading frames were amplified from *Trypanosoma brucei brucei* strain Lister 427 genomic
1123 DNA by PCR. The PCR product was digested with NdeI and XhoI restriction enzymes and
1124 ligated into the pET21-a expression vector, which encodes an N-terminal His6 tag. The plasmid
1125 was used to perform a chemical transformation into *E. coli* strain Rosetta II (DE3) pLysS.
1126 Individual colonies were subsequently grown at 37 °C in presence of 100 µg/ml ampicillin to
1127 an OD600 of ~ 0.8. Recombinant protein expression was induced by the addition of 50 µM
1128 IPTG and the cells were incubated for 4 h at 37 °C with shaking. Cells were harvested by
1129 centrifugation (3000 x *g*, 10 min, 4 °C). The pellet was resuspended in 10 ml lysis buffer (100
1130 mM NaH_2PO_4, 10 mM Tris/ HCl, 8M Urea, pH 8.0) and incubated for 1 h at RT on. Final lysis
1131 was then achieved with sonication on ice, using 6 cycles for 10 s with MiniTip step 7 (Sonifier,
1132 B-12, Branson Ultrasonics). Lysates were clarified by centrifugation (10,000 x *g*, 30 min, RT)
1133 and incubated for 1 hour with Ni-NTA His bind resin (Merck) rolling at RT. Afterwards, the
1134 resin was transferred to a HiTrap column (GE healthcare) and washed with 30 ml lysis buffer
1135 and 30 ml buffer B (100 mM NaH_2PO_4, 10 mM Tris/ HCl, 8 M Urea, pH 6.3). Next, the bound
1136 proteins were eluted with 1 x 2 ml buffer C (100 mM NaH_2PO_4, 10 mM Tris/ HCl, 8 M Urea
1137 pH, 5.9), 1 x 2ml buffer D (100 mM NaH_2PO_4, 10 mM Tris/ HCl, 8M Urea pH 4.5) and 1 x 2
1138 ml buffer E (100 mM NaH_2PO_4, 10 mM Tris/ HCl, 8 M Urea, pH 4.5 + 250 mM imidazole).

1139 All elution's were then separately dialysed overnight against a 20 mM phosphate buffer
1140 (2.7 mM Na_2HPO_4, 17.3 mM NaH_2PO_4) at 4 °C. The purification success was validated by
1141 15 % SDS-PAGE and proteins were sent to different companies for antibody generation.
1142

1143 **Antibody generation**

1144 Recombinant full-size proteins were used to immunise different animals (Pineda, Berlin,
1145 Germany; Davids Biotechnology, Regensburg, Germany; Eurogentec, Seraing, Belgium). The
1146 resulting antisera were affinity purified against the immobilised recombinant protein. The
1147 resulting antisera from two rats (anti-TbRab5A) showed no need for affinity purification. All
1148 antibodies were validated for selectivity through immunoblots of the corresponding RNAi cell
1149 line (Supplementary 2).
1150

1151 **HaloTag ligand labelling**

1152 HaloTag-Ligand-Amine (Promega, #P6741) was reconstituted in DMF (Sigma-Aldrich,
1153 #70547) to a concentration of 10 g/l. 250 µg HaloTag-Ligand Amine was conjugated to Alexa
1154 Fluor 647-NHS (Thermofisher, #A20006) by adding 150 µg of NHS-dye from a 10 g/l stock
1155 solution in DMF. The total reaction volume was adjusted to 120 µl with DMF, then DIPEA
1156 Base (Sigma-Aldrich, #387649) was added at 1:100. The reaction was incubated under gentle
1157 agitation and protected from light at room temperature for three hours. The reaction mixture
1158 was purified by reverse-phase high performance liquid chromatography (HPLC, Jasco) using a
1159 biphenyl column (Kinetex, #00F-4622-E0) with a solvent gradient of 0-60 % (v/v) acetonitrile
1160 (Sigma-Aldrich, #34851) in 0.1 % TFA (Sigma-Aldrich, #T6508) in water run over 30 min.
1161 Collected product fractions were dried in a speed-vac (Thermofisher, #SPD111V) and
1162 dissolved in DMSO.
1163

1164

1165

1166

1167

1168

1169

Acknowledgements

We thank the Cell Microscopy Core of UMC Utrecht for their workshop "Cryosectioning and immuno-electron microscopy" and the opportunity to learn the Tokuyasu technique. Manfred Alsheimer provided protocols and advice with recombinant protein expression and antibody generation. Daniela Bunsen and Claudia Gehring-Höhn provided help with the EM benchwork and assistance with the electron microscope. Bernardo Gabiatti, Janna Eilts, Marcel Rühling and Tobias Kunz provided protocols and advice on expansion microscopy. We are grateful to Brooke Morriswood for essential discussions. We express our gratitude to the eLife reviewers for dedicating their time and effort to evaluate the manuscript. We sincerely value all the insightful comments and suggestions, particularly those related to obtaining tomograms of unprocessed cells for use as a control. These recommendations played a crucial role in enhancing the overall quality of the manuscript.

Funding

ME was supported by DFG grants EN305, SPP1726 (Microswimmers—From Single Particle Motion to Collective Behaviour), GIF grant I-473-416.13/2018 (Effect of extracellular *Trypanosoma brucei* vesicles on collective and social parasite motility and development in the tsetse fly) and GRK2157 (3D Tissue Models to Study Microbial Infections by Obligate Human Pathogens), the EU ITN Physics of Motility, and the BMBF NUM Organo-Strat. ME is a member of the Wilhelm Conrad Röntgen Center for Complex Material Systems (RCCM). The transmission electron microscopes in Würzburg were funded by the Deutsche Forschungsgemeinschaft (DFG, German Research Foundation) – 426173797 (INST 93/1003-1 FUGG) and 218894163. AB was supported by the Brazilian agency CAPES (program: CAPES/DAAD—Call No. 22/2018; process 88881.199683/2018-01). MJ was supported by GRK2157 and the European Research Council (ERC) under the European Union's Horizon 2020 research and innovation programme (grant agreement No 835102) awarded to MS.

1200 **References**

1201 Ackers, J.P., Dhir, V., and Field, M.C. (2005). A bioinformatic analysis of the RAB genes of *Trypanosoma*
1202 *brucei*. Mol Biochem Parasitol *141*, 89-97.
1203 Alcantara, C.L., de Souza, W., and da Cunha, E.S.N.L. (2018). Tridimensional Electron Microscopy
1204 Analysis of the Early Endosomes and Endocytic Traffic in *Trypanosoma cruzi* Epimastigotes. Protist *169*,
1205 887-910.
1206 Allen, C.L., Goulding, D., and Field, M.C. (2003). Clathrin-mediated endocytosis is essential in
1207 *Trypanosoma brucei*. EMBO J *22*, 4991-5002.
1208 Alonso, V.L. (2022). Ultrastructure Expansion Microscopy (U-ExM) in *Trypanosoma cruzi*: localization
1209 of tubulin isoforms and isotypes. Parasitology Research *121*, 3019-3024.
1210 Alsford, S., Kawahara, T., Glover, L., and Horn, D. (2005). Tagging a *T. brucei* RRNA locus improves stable
1211 transfection efficiency and circumvents inducible expression position effects. Mol Biochem Parasitol
1212 *144*, 142-148.
1213 Amodeo, S., Kalichava, A., Fradera-Sola, A., Bertiaux-Lequoy, E., Guichard, P., Butter, F., and
1214 Ochsenreiter, T. (2021). Characterization of the novel mitochondrial genome segregation factor
1215 TAP110 in *Trypanosoma brucei*. Journal of Cell Science *134*, jcs254300.
1216 Ansari, I., Basak, R., and Mukhopadhyay, A. (2022). Hemoglobin Endocytosis and Intracellular
1217 Trafficking: A Novel Way of Heme Acquisition by *Leishmania*. Pathogens *11*.
1218 Bartossek, T., Jones, N.G., Schafer, C., Cvitkovic, M., Glogger, M., Mott, H.R., Kuper, J., Brennich, M.,
1219 Carrington, M., Smith, A.S*., et al.* (2017). Structural basis for the shielding function of the dynamic
1220 trypanosome variant surface glycoprotein coat. Nat Microbiol *2*, 1523-1532.
1221 Becker, M., Aitcheson, N., Byles, E., Wickstead, B., Louis, E., and Rudenko, G. (2004). Isolation of the
1222 repertoire of VSG expression site containing telomeres of *Trypanosoma brucei* 427 using
1223 transformation-associated recombination in yeast. Genome Res *14*, 2319-2329.
1224 Benchimol, M., and de Souza, W. (2022). *Giardia intestinalis* and its endomembrane system. Journal of
1225 Eukaryotic Microbiology *69*, e12893.
1226 Boehm, C.M., Obado, S., Gadelha, C., Kaupisch, A., Manna, P.T., Gould, G.W., Munson, M., Chait, B.T.,
1227 Rout, M.P., and Field, M.C. (2017). The Trypanosome Exocyst: A Conserved Structure Revealing a New
1228 Role in Endocytosis. PLoS Pathog *13*, e1006063.
1229 Borges, A.R., Link, F., Engstler, M., and Jones, N.G. (2021). The Glycosylphosphatidylinositol Anchor: A
1230 Linchpin for Cell Surface Versatility of Trypanosomatids. Frontiers in Cell and Developmental Biology
1231 *9*.
1232 Burki, F., Roger, A.J., Brown, M.W., and Simpson, A.G.B. (2020). The New Tree of Eukaryotes. Trends in
1233 Ecology & Evolution *35*, 43-55.
1234 Chaves, I., Rudenko, G., Dirks-Mulder, A., Cross, M., and Borst, P. (1999). Control of variant surface
1235 glycoprotein gene-expression sites in *Trypanosoma brucei*. EMBO J *18*, 4846-4855.
1236 Chen, F., Tillberg, P.W., and Boyden, E.S. (2015). Optical imaging. Expansion microscopy. Science *347*,
1237 543-548.
1238 Chi, R.J., Harrison, M.S., and Burd, C.G. (2015). Biogenesis of endosome-derived transport carriers. Cell
1239 Mol Life Sci *72*, 3441-3455.
1240 Costes, S.V., Daelemans, D., Cho, E.H., Dobbin, Z., Pavlakis, G., and Lockett, S. (2004). Automatic and
1241 quantitative measurement of protein-protein colocalization in live cells. Biophys J *86*, 3993-4003.
1242 Cross, G.A. (1975). Identification, purification and properties of clone-specific glycoprotein antigens
1243 constituting the surface coat of *Trypanosoma brucei*. Parasitology *71*, 393-417.
1244 Engstler, M., and Boshart, M. (2004). Cold shock and regulation of surface protein trafficking convey
1245 sensitization to inducers of stage differentiation in *Trypanosoma brucei*. Genes Dev *18*, 2798-2811.
1246 Engstler, M., Pfohl, T., Herminghaus, S., Boshart, M., Wiegertjes, G., Heddergott, N., and Overath, P.
1247 (2007). Hydrodynamic flow-mediated protein sorting on the cell surface of trypanosomes. Cell *131*,
1248 505-515.
1249 Engstler, M., Thilo, L., Weise, F., Grunfelder, C.G., Schwarz, H., Boshart, M., and Overath, P. (2004).
1250 Kinetics of endocytosis and recycling of the GPI-anchored variant surface glycoprotein in *Trypanosoma*
1251 *brucei*. J Cell Sci *117*, 1105-1115.

1252 Field, H., Farjah, M., Pal, A., Gull, K., and Field, M.C. (1998). Complexity of trypanosomatid endocytosis
1253 pathways revealed by Rab4 and Rab5 isoforms in *Trypanosoma brucei*. J Biol Chem *273*, 32102-32110.
1254 Gambarotto, D., Zwettler, F.U., Le Guennec, M., Schmidt-Cernohorska, M., Fortun, D., Borgers, S.,
1255 Heine, J., Schloetel, J.-G., Reuss, M., and Unser, M. (2019). Imaging cellular ultrastructures using
1256 expansion microscopy (U-ExM). Nature Methods *16*, 71-74.
1257 Gorilak, P., Pružincová, M., Vachova, H., Olšinová, M., Schmidt Cernohorska, M., and Varga, V. (2021).
1258 Expansion microscopy facilitates quantitative super-resolution studies of cytoskeletal structures in
1259 kinetoplastid parasites. Open Biology *11*, 210131.
1260 Grünfelder, C.G., Engstler, M., Weise, F., Schwarz, H., Stierhof, Y.D., Morgan, G.W., Field, M.C., and
1261 Overath, P. (2003). Endocytosis of a glycosylphosphatidylinositol-anchored protein via clathrin-coated
1262 vesicles, sorting by default in endosomes, and exocytosis via RAB11-positive carriers. Mol Biol Cell *14*,
1263 2029-2040.
1264 Gull, K. (2003). Host–parasite interactions and trypanosome morphogenesis: a flagellar pocketful of
1265 goodies. Current Opinion in Microbiology *6*, 365-370.
1266 Hall, B.S., Smith, E., Langer, W., Jacobs, L.A., Goulding, D., and Field, M.C. (2005). Developmental
1267 variation in Rab11-dependent trafficking in *Trypanosoma brucei*. Eukaryot Cell *4*, 971-980.
1268 Hartel, A.J., Glogger, M., Jones, N.G., Abuillan, W., Batram, C., Hermann, A., Fenz, S.F., Tanaka, M., and
1269 Engstler, M. (2016). N-glycosylation enables high lateral mobility of GPI-anchored proteins at a
1270 molecular crowding threshold. Nat Commun *7*, 12870.
1271 Heilemann, M., van de Linde, S., Schuttpelz, M., Kasper, R., Seefeldt, B., Mukherjee, A., Tinnefeld, P.,
1272 and Sauer, M. (2008). Subdiffraction-resolution fluorescence imaging with conventional fluorescent
1273 probes. Angew Chem Int Ed Engl *47*, 6172-6176.
1274 Hirumi, H., and Hirumi, K. (1989). Continuous cultivation of *Trypanosoma brucei* blood stream forms
1275 in a medium containing a low concentration of serum protein without feeder cell layers. J Parasitol *75*,
1276 985-989.
1277 Jones, N.G., Thomas, E.B., Brown, E., Dickens, N.J., Hammarton, T.C., and Mottram, J.C. (2014).
1278 Regulators of *Trypanosoma brucei* cell cycle progression and differentiation identified using a kinome-
1279 wide RNAi screen. PLoS Pathog *10*, e1003886.
1280 Kalichava, A., and Ochsenreiter, T. (2021). Ultrastructure expansion microscopy in *Trypanosoma*
1281 *brucei*. Open Biology *11*, 210132.
1282 Link, F., Borges, A.R., Jones, N.G., and Engstler, M. (2021). To the Surface and Back: Exo- and Endocytic
1283 Pathways in *Trypanosoma brucei*. Front Cell Dev Biol *9*, 720521.
1284 Mayor, S., Presley, J.F., and Maxfield, F.R. (1993). Sorting of membrane components from endosomes
1285 and subsequent recycling to the cell surface occurs by a bulk flow process. Journal of Cell Biology *121*,
1286 1257-1269.
1287 McGovern, O.L., Rivera-Cuevas, Y., and Carruthers, V.B. (2021). Emerging Mechanisms of Endocytosis
1288 in *Toxoplasma gondii*. Life *11*, 84.
1289 Minamino, N., and Ueda, T. (2019). RAB GTPases and their effectors in plant endosomal transport.
1290 Current Opinion in Plant Biology *52*, 61-68.
1291 Möbius, W., and Posthuma, G. (2019). Sugar and ice: Immunoelectron microscopy using cryosections
1292 according to the Tokuyasu method. Tissue Cell *57*, 90-102.
1293 Morgan, G.W., Allen, C.L., Jeffries, T.R., Hollinshead, M., and Field, M.C. (2001). Developmental and
1294 morphological regulation of clathrin-mediated endocytosis in *Trypanosoma brucei*. J Cell Sci *114*, 2605-
1295 2615.
1296 Mugnier, M.R., Stebbins, C.E., and Papavasiliou, F.N. (2016). Masters of Disguise: Antigenic Variation
1297 and the VSG Coat in *Trypanosoma brucei*. PLoS Pathog *12*, e1005784.
1298 Overath, P., and Engstler, M. (2004). Endocytosis, membrane recycling and sorting of GPI-anchored
1299 proteins: *Trypanosoma brucei* as a model system. Mol Microbiol *53*, 735-744.
1300 Overath, P., Stierhof, Y.D., and Wiese, M. (1997). Endocytosis and secretion in trypanosomatid
1301 parasites - Tumultuous traffic in a pocket. Trends Cell Biol *7*, 27-33.
1302 Pal, A., Hall, B.S., Jeffries, T.R., and Field, M.C. (2003). Rab5 and Rab11 mediate transferrin and anti-
1303 variant surface glycoprotein antibody recycling in *Trypanosoma brucei*. Biochem J *374*, 443-451.

Podinovskaia, M., Prescianotto-Baschong, C., Buser, D.P., and Spang, A. (2021). A novel live-cell imaging assay reveals regulation of endosome maturation. Elife *10*.

Podinovskaia, M., and Spang, A. (2018). The Endosomal Network: Mediators and Regulators of Endosome Maturation. In Endocytosis and Signaling, C. Lamaze, and I. Prior, eds. (Cham: Springer International Publishing), pp. 1-38.

Porto-Carreiro, I., Attias, M., Miranda, K., De Souza, W., and Cunha-e-Silva, N. (2000). *Trypanosoma cruzi* epimastigote endocytic pathway: cargo enters the cytostome and passes through an early endosomal network before storage in reservosomes. Eur J Cell Biol *79*, 858-869.

Poteryaev, D., Datta, S., Ackema, K., Zerial, M., and Spang, A. (2010). Identification of the switch in early-to-late endosome transition. Cell *141*, 497-508.

Redmond, S., Vadivelu, J., and Field, M.C. (2003). RNAit: an automated web-based tool for the selection of RNAi targets in *Trypanosoma brucei*. Mol Biochem Parasitol *128*, 115-118.

Rink, J., Ghigo, E., Kalaidzidis, Y., and Zerial, M. (2005). Rab conversion as a mechanism of progression from early to late endosomes. Cell *122*, 735-749.

Rose, C., Casas-Sánchez, A., Dyer, N.A., Solórzano, C., Beckett, A.J., Middlehurst, B., Marcello, M., Haines, L.R., Lisack, J., Engstler, M.*, et al.* (2020). *Trypanosoma brucei* colonizes the tsetse gut via an immature peritrophic matrix in the proventriculus. Nature Microbiology *5*, 909-916.

Schwebs, M., Paul, T., Glogger, M., Forster, L., Morriswood, B., Teßmar, J., Groll, J., Engstler, M., Kollmannsberger, P., and Fenz, S. (2022). Single-molecule fluorescence microscopy demonstrates fast dynamics of the variant surface glycoprotein coat on living trypanosomes. bioRxiv, 2022.2008.2003.502583.

Silverman, J.S., Schwartz, K.J., Hajduk, S.L., and Bangs, J.D. (2011). Late endosomal Rab7 regulates lysosomal trafficking of endocytic but not biosynthetic cargo in *Trypanosoma brucei*. Mol Microbiol *82*, 664-678.

Slot, J.W., and Geuze, H.J. (2007). Cryosectioning and immunolabeling. Nat Protoc *2*, 2480-2491.

Stoorvogel, W., Strous, G.J., Geuze, H.J., Oorschot, V., and Schwartz, A.L. (1991). Late endosomes derive from early endosomes by maturation. Cell *65*, 417-427.

Strassert, J.F.H., Irisarri, I., Williams, T.A., and Burki, F. (2021). A molecular timescale for eukaryote evolution with implications for the origin of red algal-derived plastids. Nat Commun *12*, 1879.

Taylor, J.E., and Rudenko, G. (2006). Switching trypanosome coats: what's in the wardrobe? Trends in Genetics *22*, 614-620.

Tazeh, N.N., Silverman, J.S., Schwartz, K.J., Sevova, E.S., Sutterwala, S.S., and Bangs, J.D. (2009). Role of AP-1 in developmentally regulated lysosomal trafficking in *Trypanosoma brucei*. Eukaryot Cell *8*, 1352-1361.

Tillberg, P.W., Chen, F., Piatkevich, K.D., Zhao, Y., Yu, C.C., English, B.P., Gao, L., Martorell, A., Suk, H.J., Yoshida, F.*, et al.* (2016). Protein-retention expansion microscopy of cells and tissues labeled using standard fluorescent proteins and antibodies. Nat Biotechnol *34*, 987-992.

Triggs, V.P., and Bangs, J.D. (2003). Glycosylphosphatidylinositol-dependent protein trafficking in bloodstream stage *Trypanosoma brucei*. Eukaryot Cell *2*, 76-83.

van der Beek, J., de Heus, C., Liv, N., and Klumperman, J. (2021). Quantitative correlative microscopy reveals the ultrastructural distribution of endogenous endosomal proteins. Journal of Cell Biology *221*.

Vines, J.H., and King, J.S. (2019). The endocytic pathways of *Dictyostelium discoideum*. Int J Dev Biol *63*, 461-471.

Wirtz, E., Leal, S., Ochatt, C., and Cross, G.A. (1999). A tightly regulated inducible expression system for conditional gene knock-outs and dominant-negative genetics in *Trypanosoma brucei*. Mol Biochem Parasitol *99*, 89-101.